



# Analysis and Design of a MuSiC-Based Angle of Arrival Positioning System

MARCO GUNIA, ADRIAN ZINKE, NIKO JORAM, and FRANK ELLINGER,

Technische Universität Dresden

In this research article, a concept for a secondary RAdio Direction And Ranging (RADAR) angle of arrival based system with cooperative targets transmitting at 2.4 GHz and using Multiple Signal Classification (MuSiC) to determine the angles of incidence is investigated. In addition to introducing common algorithms and presenting thorough derivations, the system is first examined through simulations. To prove the concept, hardware, firmware, and software are developed. For MuSiC, we propose three novel methods to obtain the correct incident angle from the spectrum, especially in strong multipath environments. These methods work either for a single spectrum or for a combination recorded at multiple times. Together with the estimated angles of incidence, our methods determine measures on the respective likelihoods. Based on this, we additionally propose two algorithms for computing the final position. Our system is characterized in both a simple 20 m × 15 m outdoor and a 17 m × 13 m multipath indoor environment, where we achieve a mean angular error of 3° and a mean positioning error of 0.67 m for the former using only four base stations with four antennas each. Our novel approach shows position accuracy improvements of 15% outdoors and 25% indoors compared to classical MuSiC estimation.

CCS Concepts: • Networks → Location based services; • Information systems → Location based services; • Computer systems organization → Firmware; Embedded hardware; Embedded software;

Additional Key Words and Phrases: Positioning, localization, angle of arrival, AoA, incident angle, direction of arrival, DoA, secondary RADAR, Fast Fourier Transform, FFT, multiple signal classification, MuSiC, phase difference, spectrum, weighting, relevance, quality, area ratio

## ACM Reference format:

Marco Gunia, Adrian Zinke, Niko Joram, and Frank Ellinger. 2023. Analysis and Design of a MuSiC-Based Angle of Arrival Positioning System. *ACM Trans. Sensor Netw.* 19, 3, Article 66 (March 2023), 41 pages.

<https://doi.org/10.1145/3577927>

66

## 1 INTRODUCTION

Most of today's positioning systems are somehow based on determining ranges to some reference, such as to multiple **Base Stations (BS)**. For common outdoor installations like the GPS (Global Positioning System), GLONASS (Global Navigation Satellite System), or Galileo, the position of

---

This project received funding from the ECSEL Joint Undertaking (JU) under grant agreement 876487. The JU receives support from the European Union's Horizon 2020 research and innovation programme and Finland, Spain, Italy, Germany, Czech Republic, Belgium, and Netherlands.

Authors' address: M. Gunia (corresponding author), A. Zinke, N. Joram, and F. Ellinger, Technische Universität Dresden, Dresden, 01062, Germany; emails: marco.gunia@tu-dresden.de, post@adrian-zinke.de, {niko.joram, frank.ellinger}@tu-dresden.de.



[This work is licensed under a Creative Commons Attribution International 4.0 License.](#)

© 2023 Copyright held by the owner/author(s).

1550-4859/2023/03-ART66

<https://doi.org/10.1145/3577927>

a device is computed from distances to various satellites. Likewise, many indoor setups also are employing ranges. On the one hand, this is true for very simple low-priced systems based on **Wireless Local Area Networks (WLAN)** or Bluetooth, where a one-to-one relation between signal strength and distance is exploited. On the other hand, even in very sophisticated frequency modulated continuous wave **RADAR Direction And Ranging (RADAR)** or ultra-wideband RADAR, an intermediate range result is derived. **Inertial Navigation Systems (INS)** are operating differently from the preceding by using accelerometers or gyroscopes, but they still determine distances either by employing step recognition or by double-integrating acceleration data to come up with a position relative to a starting point.

A completely different approach is to employ the angle of the incident signal as an intermediate result. Especially for hybrid structures, this provides another quantity that can be used to improve the estimate of classical ranging-based techniques in strong multipath environments.

Many of the systems seeking for the incident angle derive the estimate by maximum search in a spectrum. Especially in scenarios where multipath is likely to occur, these simple approaches lead to poor performance. In this regard, this article proposes new methods for estimating the incident angle. Moreover, we present techniques to easily apply these results for positioning. In contrast to many publications, we investigate our ideas experimentally in realistic settings.

The system developed within this work consists of various BS, where each employs multiple independent non-coherent **Commercial-Off-The-Shelf (COTS)** radio transceivers. The BS, whose position is sought, is transmitting sinusoidal waves, being simultaneously received by the other BS at a known location. These identify the incident angles by recording the respective I/Q-data and performing the **Fast Fourier Transform (FFT)** or **Multiple Signal Classification (MuSiC)** that finally enables position calculation.

In the following, customized hardware is designed for the following reasons. First, related works are either simulation only (e.g., [13, 46, 57, 61]) or is based on standard hardware. The latter subdivides in approaches utilizing the **Channel State Information (CSI)** of standard **Network Interface Cards (NIC)** (e.g., [31, 54]) or expensive specialized COTS modules at high cost (e.g., [11]). Although CSI is not primary tailed for determining the incident angle but the properties of the channel, specialized COTS hardware can easily consume several thousand dollars. As an example, the WBX daughterboards from Ettus Research in the work of Chen et al. [11] cost around \$5,000 for each BS. In contrast, the total price of all our setup is equal to the aforementioned value. Additionally, both options require setting up a bulky host PC for signal processing, which is not required in our work, since all calculations are carried out within an embedded system. Recently, there have been efforts in exploiting low-budget Internet of Things devices, which neither feature CSI nor multiple antennas. In this regard, research deals with how to enable CSI (e.g., [38]), as well as to support various antennas as in the work of Hu et al. [25]. Nevertheless, accuracy is often only moderate. Second, a user-specific design enables optimization of the hardware and firmware with respect to the envisaged software for signal processing. As a last benefit, a custom interface allows us to use that entity together with other localization means within our hybrid positioning solution being introduced in previous work [19–21]. However, the novel algorithms not only are applicable to our particular hardware but also are easily employed for any means based on analyzing spectra. Thus, we investigate an **Angle of Arrival (AOA)** based positioning approach for secondary RADAR covering all aspects from theory up to system design within this research work.

We start by introducing related work in Section 2. The mathematical and signal basics are presented in Section 3. Here, we demonstrate the principles starting by ideal coherent reception with two antennas. These preconditions are weakened stepwise to finally support non-coherent receivers being used within our envisaged system. For deriving the incident angle, we direct our research toward the MuSiC algorithm in Section 4. In that regard, the text contains comprehensive

Table 1. Classification of AoA Algorithms

	Classical	Subspace Based
Parametric	<ul style="list-style-type: none"> <li>• Reference signal</li> <li>• Correlation</li> </ul>	<ul style="list-style-type: none"> <li>• Root-MuSiC [6]</li> <li>• ESPRIT [52]</li> </ul>
Spectral	<ul style="list-style-type: none"> <li>• Bartlett [7]</li> <li>• Capon [8]</li> <li>• Linear prediction [39]</li> <li>• Maximum entropy [17]</li> <li>• SBS and XSBS [4]</li> <li>• FFT [14]</li> </ul>	<ul style="list-style-type: none"> <li>• MuSiC [53]</li> <li>• Smooth-MuSiC [55]</li> <li>• Cyclic-MuSiC [15]</li> <li>• Min-norm [33, 51]</li> <li>• Pisarenko harmonic decomposition [49]</li> </ul>

derivations, including some theoretical proofs on the complex signal covariance matrices in the appendix, which on the best knowledge of the authors are not found in the literature. Related work mostly assumes non-complex behavior, which is not correct since I/Q-data is complex. For comparison, this section contains some additional content on the FFT, being a simple alternative approach. In Section 5, our three novel methods to obtain the incident angles from the MuSiC spectrum are proposed. Building on that, two algorithms to determine the final position estimate are introduced in Section 6. In Section 7, we execute simulations to deduce the system specification. To support the theoretical aspects, the system design including hardware, firmware, and software is carried out in Section 8. For proving the concepts, we characterize our AoA-based secondary RADAR system in Section 9 in an outdoor and a multipath indoor environment. The article closes with a conclusion and an outlook. Some preliminary works on detecting the incident angle for coherent receivers (Section 3.1) and on hardware design (Section 8.1) were published previously [22].

In the further course of this article, we use the following designators. A scalar is denoted by a lower italic letter, whereas a vector is additionally written in bold (e.g.,  $\mathbf{b}$ ). Matrices employ bold italic capital letters (e.g.,  $\mathbf{B}$ ). Constants are handled equally but in contrast are written in non-italic form. To better distinguish scalar constants, we often use capital letters (e.g., N). The symbol  $\tilde{\cdot}$  indicates random variables (e.g.,  $\tilde{x}$ ) and the prefix  $E\cdot$  is used to characterize an estimator, which is generally also a random variable (e.g.,  $E\tilde{x}$ ). Complex variables are secondarily underlined. As an example, in the following we utilize the index  $\triangleleft\bullet$  to specify the incident angle to a **Mobile Station (MS)**, being that entity whose position is sought. Thus,  $\alpha_{\triangleleft\bullet}$  identifies the true incident angle, whereas  $\tilde{\alpha}_{\triangleleft\bullet}$  refers to its associated random variable. To highlight its nature as an estimator, we use in particular  $E\tilde{\alpha}_{\triangleleft\bullet}$ .

## 2 RELATED WORK

This section summarizes related work. Based on a classification, a multitude of AoA algorithms are introduced initially. Subsequently, the text is directed toward presenting real working systems. Here, we put a special emphasis on methods for reading out incident angles from spectra. The section concludes with a presentation of alternative maximum detection and grouping techniques.

### 2.1 Classification of AoA Algorithms

Table 1 classifies AoA algorithms into four different groups by means of two distinct features. The first feature, introduced in the work of Abusultan et al. [2], distinguishes parametric and spectral algorithms, depending on the procedure in which the incident angle is derived. Parametric variants solve equation systems or optimize parameters to calculate the value directly. In contrast, spectral methods estimate a pseudo-spectrum showing power, amplitude, or signal strength as a function of

the angle and seek the argument for the maximum. Orthogonally, the approaches can be classified into classical- and subspace based as proposed in the work of Badawy et al. [4, 5]. Classical-based methods condense all variants either utilizing the principles from Section 3 as well as approaches adjusting the direction of the beams, such as by applying antenna characteristics or by digitally controlling antenna arrays. In contrast, subspace-based methods determine the signal and noise subspace by singular value decomposition of the correlation matrix calculated from the receiving signal matrix. In the following, these algorithms are presented in turn.

**2.1.1 Classical Parametric Approaches.** One classical method is to send out a sinusoidal reference signal from a station, which is received by a multi-antenna receiver. The incident angle is then derived by considering the phase relations of the received signals at the antennas. This method is introduced in detail in Sections 3.1, 3.2, and 3.4 for coherent, non-coherent, and quasi-coherent reception, respectively. Advantageous is its low complexity. However, the nature of the signal considered being sinusoidal, the limitation to only one sending source at a time, and its susceptibility to frequency deviations of the reference are drawbacks.

Correlation is an extension toward arbitrary sending signals, which is presented in Section 3.5. Besides supporting arbitrary signals, it is not sensitive to frequency deviations of the sender. The latter is due to the fact that processing does not depend on the sinusoidal nature of the signal, and thus there is no reference frequency.

**2.1.2 Classical Spectral Approaches.** Bartlett [7] can be considered a natural extension to the correlation method. In contrast to determining the time difference for propagating from one receiving antenna to the next, Bartlett derives phase shifts resulting from these time differences as highlighted in the work of Abusultan et al. [2]. In particular, let there be  $M$  receiving antennas. For every angle  $\alpha_{\triangleleft i}$  of interest, a steering vector  $s(\alpha_{\triangleleft i}) = [1, s_2(\alpha_{\triangleleft i}), s_3(\alpha_{\triangleleft i}), \dots, s_M(\alpha_{\triangleleft i})]^T$  is generated, being a vector containing ideal phase differences from the  $i$ -th antenna to the first antenna. Subsequently, a weight vector, which can be considered a spatial filter [29], is derived and upon that a spatial spectrum is made up. The estimated angle is the one with maximum value in the spectrum for all angles  $\alpha_{\triangleleft i}$  of interest. Capon [8] is an enhanced version, where the weights are calculated by minimizing the power of the signals not being in the direction of the angle of interest  $\alpha_{\triangleleft i}$ . Therefore, the signal correlation matrix is set up. In contrast to Bartlett, it enables higher angular resolution, especially to separate sources being located closer than the beamwidth [29], but fails to work on strong correlated signals [65]. Based on that, there are further alternative variants, mainly differing in the definition of the weights, such as linear prediction [39] or maximum entropy [17].

**Switched Beam Systems (SBS)** alternatively choose between several available radiation patterns. They consist of multiple receiving antennas, potentially arranged as a linear array, being connected to a single receiver **Integrated Circuit (IC)** via a beamforming network. The beamforming network weights the input of every antenna and generates its sum. By modifying the weights, different radiation patterns are generated. The angle of the main lobe of the antenna pattern with the highest received power is used as the estimate. The advantage of simplicity (i.e., solely a single receiver IC is employed and no signal processing must be performed) contrasts with the disadvantage of only utilizing a discrete set of possible radiation patterns being equal to a discrete set of possible angles. Another drawback is failing at a low **Signal to Noise Ratio (SNR)** [18]. On this account, there are approaches coping with low SNR, such as the **Cross-correlation Switched Beam System (XSBS)** [4].

Employing the FFT is a simple approach, where transformation to Fourier space is only performed to determine the associated phase of the significant frequency [14].

**2.1.3 Subspace-Based Spectral Approaches.** MuSiC, which is introduced in Section 4.2, initially sets up the signal and noise subspace. After that, a pseudo-spectrum is compiled, where the angles of the incident signals are retrieved. Smooth-MuSiC [55] and Cyclic-MuSiC [15] also belong to this category. Whereas the former is intended to be used for strong correlated signals by pre-processing the received data [50], the latter is tailored for cyclostationary signals, particularly for settings where the recording of periodic signals at all antennas cannot be performed in parallel [64]. The reduced hardware effort is an advantage of Cyclic-MuSiC; however, its use is limited due to its signal requirements. For Smooth-MuSiC, the application to handle strong correlated signals contrasts with the reduction in the amount of distinguishable signals [28]. Besides MuSiC, there are many further algorithms estimating the spectrum, such as Min-norm [33, 51] or Pisarenko harmonic decomposition [49].

**2.1.4 Subspace-Based Parametric Approaches.** ESPRIT [52] is a method where the assembly of the signal space is accomplished by means of singular value decomposition, similar to MuSiC, employing an initially calculated correlation matrix of the received signals. ESPRIT requires that the arrangement of the antennas is such that it can be considered as set of distinct antenna pairs, where the second antenna exhibits the same orientation and distance to the first antenna for every pair. In doing so and assuming far-field, the incident angle must be identical for every pair and can be calculated directly from the eigenvalues [52]. Compared to MuSiC, the complexity is lower, since the incident angles are determined straightforward and not by seeking the spectrum. However, ESPRIT requires more antennas to clearly distinguish between a fixed amount of simultaneous senders, and its performance is slightly worse [34]. Hence, ESPRIT is suitable for systems suffering from low processing power but offering high antenna counts.

Root-MuSiC [6] is similar to MuSiC, except that the denominator in the spectrum<sup>1</sup> is approximated by a polynomial. Finding the roots of this polynomial is equivalent to seeking the maxima in the spectrum, simplifying processing. However, Root-MuSiC is only applicable for arrangements of collinear antennas with equal spacing, denoted as **Uniform Linear Arrays (ULA)**.

## 2.2 AoA-Based Systems

For calculating a position by means of multiple distance or angle measurements, various algorithms can be applied. A general overview including iterative and least squares as well as their weighted variants is given in the work of Tarrio et al. [60]. In particular, approaches employing least squares or weighted least squares utilizing the incident angle are introduced by Chan et al. [9]. Another common procedure is maximum likelihood, which is used in the work of Wang et al. [63] and Gazzah et al. [16]. Either individual or as a combination, these algorithms are generally included in some way in the complete systems presented next.

An iterative approach, where the incident angles to different BS are employed, is that of Torreieri [61]. Here, the non-linear equation system is first linearized by Taylor-series expansion and afterward solved by maximum likelihood. Until convergence, these two steps are repeated, with the maximum likelihood result serving as a new starting point for linearization. Building on that, Pages-Zamora et al. [46] propose a non-iterative closed-form solution. Their simulations reveal that the iterative approach is superior, although convergence is not always guaranteed. Cheung et al. [13] extend the work of Torrieri [61] to utilizing weighted least squares instead of maximum likelihood. There are other similar algorithms (e.g., [57]) that uses constrained least squares. However, neither Cheung et al. [13], Pages-Zamora et al. [46], and Torrieri [61] nor Sun et al. [57] are investigating or using real hardware.

---

<sup>1</sup>The spectrum is derived in Equation (26).

A system utilizing COTS **Software-Defined Radios (SDR)** is described by Chen et al. [11]. They apply the reference signal method for non-coherent receivers (introduced in Section 3.2), since the phase offsets of the SDR are not aligned. Only performing outdoor measurements, the estimate of the position is calculated by maximum likelihood. Our approach is similar, since our transceivers are also working non-coherently. However, we are not using off-the-shelf nodes but design our own hardware. Additionally, we turned away from the very simple reference method and employ FFT or MuSiC. Moreover, we propose schemes to extract the angles from spectra together with some probability being later used in a weighted positioning algorithm.

Liu et al. [38] present a system specifically tailored for Internet of Things devices based on **Long Range (LoRa)** wide area networks. To improve the overall bandwidth of the individual non-overlapping narrow frequency bands, a combination technique is proposed by utilizing fictitious bridging channels. The incident angle is determined by ESPRIT by means of introducing virtual antennas. Maximum likelihood is finally applied to calculate the position.

With the aim for a mobile robot to track targets by means of determining the corresponding angle, Hu et al. [25] propose to calculate this value by utilizing the difference of two sequential LoRa time of flight measurements of an arrangement of two antennas connected to a single radio channel via a switch. To increase accuracy, this antenna structure is rotated to create a virtual circular array. Due to its mechanical moving elements, the system is primarily intended for robotics.

Sen et al. [54] propose to use the CSI from a standard Atheros 9390 NIC to obtain the incident angle to a transmitter. By entering CSI readings into MuSiC, several possible angles can be retrieved, employing dead reckoning to select the most likely direct path. Unlike our system, they do not determine the most probable angle from the spectrum alone but are supported by additional position information from an INS. Since the data must be obtained from both sources, adaptation to other applications is made more difficult. Moreover, the system is only applicable to humans, as it uses step recognition. Their system comes with the benefit that no hardware and firmware design is carried out, whereas this article presents all steps involved.

A similar approach utilizing CSI for MuSiC is characterized in the work of Kotaru et al. [31], where standard Intel 5300 WLAN NICs are employed. Instead of being assisted by INS data, they derive the distance of the direct path via the received signal strength. The final position is calculated by examining a user-defined likelihood function of the two measures, first clustering them. Again, there are no investigations in selecting the most probable angle solely from the spectrum. Since an additional source of information is again required, this solution suffers from the same drawbacks as the work of Sen et al. [54].

To the best of our knowledge, there are no publications on seeking for the most probable angle in the MuSiC spectrum alone. However, most sources are satisfied with the search for the highest peak (e.g., [12, 30, 58]). Nevertheless, the latter uses some kind of clustering to identify multiple sources. However, we are dealing with the different problem of finding one source, where there are multiple peaks in the spectrum due to multipath. Other alternative peak detection and clustering techniques are listed in the following.

### 2.3 Peak Detection and Clustering Techniques

Especially for ultra-wideband positioning, maximum detection is used to identify the first signal energy corresponding to the direct path. The DW1000 from Decawave, described in the work of Neirynck et al. [41], is one of the first COTS ICs employing such a leading edge detection algorithm. Unfortunately, this algorithm is implemented in encrypted form by the manufacturer as firmware in a special part of the circuit. Already some years ago, a comparison of different approaches based on threshold detection was carried out by Haneda et al. [23]. In contrast, an advanced variant is introduced in the work of Kuhn et al. [32] that uses a processing sequence

consisting of moving average, maximum search within a window of fixed size, and threshold comparison.

RADAR for surveillance applications, which cope with identifying targets against background noise, are evaluated by means of the constant false alarm rate metric. An analysis of multiple of these techniques, which operate on forming adaptive thresholds on reference windows, is carried out in the work of Xiangwei et al. [66].

Clustering in the work of Kotaru et al. [31], presented in the last section, is performed with the goal of determining the variance of the incidence angle and time of flight across multiple measurements for similar propagation paths. With the intention that the signal path with the smallest variation is the direct path, a likelihood function is established for each of these clusters that is inversely proportional to the variance of the measurements. A Gaussian mean clustering algorithm with five clusters is used, since the authors assume that there are at best five significant paths in an indoor environment. In contrast, our novel methods are not limited to a predetermined number of groups. Moreover, our approaches do not refer to the variance of the measurements but to the appearance of the spectra.

Besides the publications mentioned previously, there are other approaches where clustering is a tool for positioning and tracking. For example, machine learning is used by Islam and Nirjon [27] to predict gestures and movements by means of changes in WLAN CSI. In addition to that input, another video signal is recorded during training, and both sources are subsequently clustered in a feature space.

### 3 PRINCIPLE FOR DETERMINING THE AOA

This section studies general principles for determining the incident angle depending on the hardware available. After initially investigating coherent receivers with two antennas on sinusoidal signals, these assumptions are gradually reduced to subsequently characterize non-coherent receivers with multiple antennas, the latter being used in our system. We conclude with some remarks on quasi-coherent behavior as well as on arbitrary signals, which are not used in this work.

To easily identify signals and variables, the following notation is used. The location of occurrence of a variable is characterized by a frame around a character subscript, such as  $\underline{S}$  for the occurrence at the sending node S. Signals often involve transmissions, which are distinguished by an arrow subscript. As an example,  $\underline{S} \rightarrow R$  indicates a transmission from a sender S to a receiver R, where the signal is considered at the sender. Often, another subscript is introduced in the context to indicate its nature, such as rf for a variable or signal at radio frequency.

#### 3.1 Coherent Receivers

First, the general principle for coherent receiving is presented by means of Figure 1. Let S be a sending node, transmitting a sinusoidal signal (index: rf) with amplitude  $A_{rf,\underline{S}}(t)$  and frequency  $f_{rf,S}$

$$s_{rf,\underline{S} \rightarrow R}(t) = \underbrace{A_{rf,\underline{S}}(t)}_{:=1} \sin(2\pi f_{rf,\underline{S}} t + \varphi_{rf,\underline{S}}) \quad (1)$$

where without loss of generality we assume  $A_{rf,\underline{S}}(t) = 1$ , since we are only interested in the phase information. Let R be a two-antenna node, whose antennas are separated by distance  $a$ , as shown in Figure 2. Assuming far-field, the signal received at first antenna (index:  $\underline{R}_1$ ) is plane-wave and reads

$$s_{rf,S \rightarrow \underline{R}_1}(t) = \sin\left(2\pi f_{rf,\underline{S}} \left[t - \frac{d_1}{c}\right] + \varphi_{rf,\underline{S}}\right). \quad (2)$$

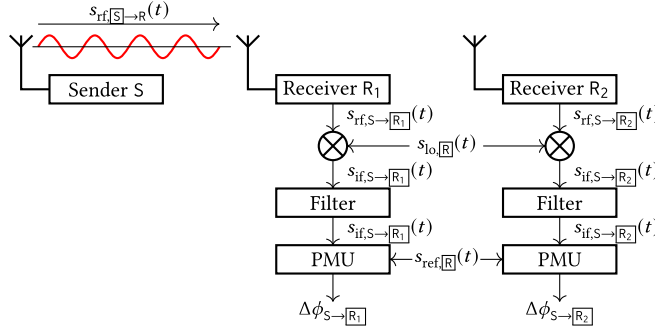


Fig. 1. Coherent receiving sinusoidal wave.

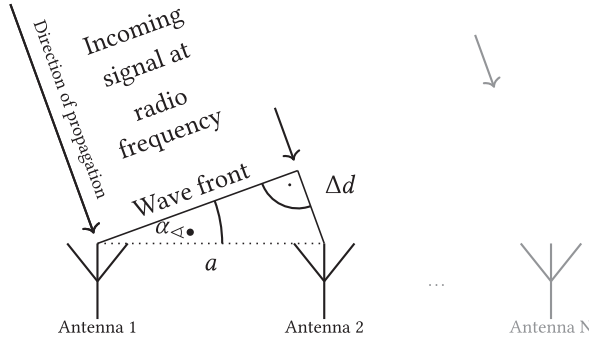


Fig. 2. Wave front of signal at radio frequency.

As indicated in that picture, the signal travels an additional distance  $\Delta d$  to the second antenna

$$\Delta d = a \sin(\alpha_{\leftarrow\rightarrow}) \quad (3)$$

being equivalent to an additional propagation time  $\Delta d/c$ . Thus, we have for the received signal at antenna 2 (index:  $[R_2]$ )

$$s_{rf,S\rightarrow[R_2]}(t) = \sin\left(2\pi f_{rf,[S]} \left[t - \frac{d_1}{c} - \frac{\Delta d}{c}\right] + \varphi_{rf,[S]}\right). \quad (4)$$

Since we initially assume coherent reception, both signals are down-converted employing the same local oscillator (index:  $lo$ )

$$s_{lo,[R]}(t) = \sin\left(2\pi f_{lo,[R]} t + \varphi_{lo,[R]}\right) \quad (5)$$

and subsequently the higher-frequency components are filtered. We described both in previous work [21]. Hence, the down-converted and filtered signals with intermediate frequency (index:  $if$ ) read

$$\begin{aligned} s_{if,S\rightarrow[R_1]}(t) &= \sin\left(2\pi f_{if,[R]} t - 2\pi f_{rf,[S]} \left[\frac{d_1}{c}\right] + \varphi_{rf,[S]} - \varphi_{lo,[R]} + \frac{\pi}{2}\right) \\ s_{if,S\rightarrow[R_2]}(t) &= \sin\left(2\pi f_{if,[R]} t - 2\pi f_{rf,[S]} \left[\frac{d_1}{c} + \frac{\Delta d}{c}\right] + \varphi_{rf,[S]} - \varphi_{lo,[R]} + \frac{\pi}{2}\right) \end{aligned} \quad (6)$$

where  $f_{\text{if},[\mathbb{R}]} := f_{\text{rf},[\mathbb{S}]} - f_{\text{lo},[\mathbb{R}]}$ . Afterward, these signals are compared to a local reference  $s_{\text{ref},[\mathbb{R}]}(t)$  with equal frequency

$$s_{\text{ref},[\mathbb{R}]}(t) = \sin(2\pi f_{\text{ref},[\mathbb{R}]} t + \varphi_{\text{ref},[\mathbb{R}]}) \quad ; \quad f_{\text{ref},[\mathbb{R}]} := f_{\text{if},[\mathbb{R}]} \quad (7)$$

within a **Phase Measurement Unit (PMU)** to obtain phase differences  $\Delta\phi_{\text{S}\rightarrow[\mathbb{R}_n]}$  at both antennas ( $n = 1, 2$ ) as explained in the work of Pelka et al. [48]. Doing so, we have

$$\begin{aligned} \Delta\phi_{\text{S}\rightarrow[\mathbb{R}_1]} &= -2\pi f_{\text{rf},[\mathbb{S}]} \left[ \frac{d_1}{c} \right] + \varphi_{\text{rf},[\mathbb{S}]} - \varphi_{\text{lo},[\mathbb{R}]} + \frac{\pi}{2} - \varphi_{\text{ref},[\mathbb{R}]} \\ \Delta\phi_{\text{S}\rightarrow[\mathbb{R}_2]} &= -2\pi f_{\text{rf},[\mathbb{S}]} \left[ \frac{d_1}{c} + \frac{\Delta d}{c} \right] + \varphi_{\text{rf},[\mathbb{S}]} - \varphi_{\text{lo},[\mathbb{R}]} + \frac{\pi}{2} - \varphi_{\text{ref},[\mathbb{R}]} \end{aligned} \quad (8)$$

A formula for the incident angle  $\alpha_{\triangleleft\bullet}$  is obtained by subtracting these phase differences

$$\Delta\phi_{\text{S}\rightarrow[\mathbb{R}_1]} - \Delta\phi_{\text{S}\rightarrow[\mathbb{R}_2]} = 2\pi f_{\text{rf},[\mathbb{S}]} \frac{\Delta d}{c} = 2\pi f_{\text{rf},[\mathbb{S}]} \frac{d \sin(\alpha_{\triangleleft\bullet})}{c} \quad (9)$$

where Equation (3) was used. Reordering, we obtain the angle

$$\sin(\alpha_{\triangleleft\bullet}) = \frac{c (\Delta\phi_{\text{S}\rightarrow[\mathbb{R}_1]} - \Delta\phi_{\text{S}\rightarrow[\mathbb{R}_2]})}{2\pi f_{\text{rf},[\mathbb{S}]} d}. \quad (10)$$

It is only mentioned in passing that the local oscillator and reference frequency in practical systems are usually derived from the same internal clock signal. Thus, frequency drifts in the local oscillator are reflected by the reference frequency and are therefore cancelled according to Equation (8). Earlier, we initially made the assumption of coherent reception, which is removed in the next paragraph.

### 3.2 Non-Coherent Receivers

If there is no common local oscillator, such as in the case of having two independent receiver ICs, the preceding coherence-assumption does not hold. Thus, instead of Equation (5), we have

$$s_{\text{lo},[\mathbb{R}_n]}(t) = \sin(2\pi f_{\text{lo},[\mathbb{R}_n]} t + \varphi_{\text{lo},[\mathbb{R}_n]}) \quad ; \quad n = 1, 2 \quad (11)$$

assuming equal frequency  $f_{\text{lo},[\mathbb{R}]}$  but differing phase angle. Moreover, the local reference according to Equation (5) is modified

$$s_{\text{ref},[\mathbb{R}_n]}(t) = \sin(2\pi f_{\text{ref},[\mathbb{R}]} t + \varphi_{\text{ref},[\mathbb{R}_n]}) \quad ; \quad n = 1, 2 \quad (12)$$

and thus  $f_{\text{ref},[\mathbb{R}]} := f_{\text{if},[\mathbb{R}]} = f_{\text{rf},[\mathbb{S}]} - f_{\text{lo},[\mathbb{R}]}$  is equal in both cases. Continuing, Equation (8) now reads

$$\begin{aligned} \Delta\phi_{\text{S}\rightarrow[\mathbb{R}_1]} &= -2\pi f_{\text{rf},[\mathbb{S}]} \left[ \frac{d_1}{c} \right] + \varphi_{\text{rf},[\mathbb{S}]} - \varphi_{\text{lo},[\mathbb{R}_1]} + \frac{\pi}{2} - \varphi_{\text{ref},[\mathbb{R}_1]} \\ \Delta\phi_{\text{S}\rightarrow[\mathbb{R}_2]} &= -2\pi f_{\text{rf},[\mathbb{S}]} \left[ \frac{d_1}{c} + \frac{\Delta d}{c} \right] + \varphi_{\text{rf},[\mathbb{S}]} - \varphi_{\text{lo},[\mathbb{R}_2]} + \frac{\pi}{2} - \varphi_{\text{ref},[\mathbb{R}_2]} \end{aligned} \quad (13)$$

and thus instead of Equation (9) we obtain

$$\Delta\phi_{\text{S}\rightarrow[\mathbb{R}_1]} - \Delta\phi_{\text{S}\rightarrow[\mathbb{R}_2]} = 2\pi f_{\text{rf},[\mathbb{S}]} \frac{d \sin(\alpha_{\triangleleft\bullet})}{c} + \underbrace{(\varphi_{\text{lo},[\mathbb{R}_2]} - \varphi_{\text{lo},[\mathbb{R}_1]} + \varphi_{\text{ref},[\mathbb{R}_2]} - \varphi_{\text{ref},[\mathbb{R}_1]})}_{\varphi_{\text{Offset}}}. \quad (14)$$

Reordering, we finally get

$$\sin(\alpha_{\triangleleft\bullet}) = \frac{c(\Delta\phi_{S \rightarrow R_1} - \Delta\phi_{S \rightarrow R_2} - \varphi_{\text{offset}})}{2\pi f_{\text{rf}[S]} d} \quad (15)$$

with unknown  $\varphi_{\text{offset}}$ , not being cancelled as before. This offset must be determined by calibration before measurement. Multiple methods are described in the work of Chau et al. [10]. One possibility, proposed by Chen et al. [11], is to initially involve an external calibrator station at a known position (i.e., with known angle  $\alpha_{\triangleleft\bullet}$ ).  $\varphi_{\text{offset}}$  is obtained by inserting that angle in Equation (15) and reordering. Self-calibration is another method, with the advantage that placing the receivers with respect to the calibrator can be dynamic. In that case, the calibration signal is generated by the system itself, such as by providing an additional sending antenna at the receiver. Alternatively, if there are at least three receiving antennas, one of these could be used for sending the calibration signal, where the remaining are used for determining the phase offsets. To identify all offsets, each antenna must in turn be employed as a calibrator. However, this is only feasible if the transceivers are able to switch between send and receive without changing the phase of the local oscillator and the reference. Another drawback is that receiving antennas are most likely in the near-field [10], invalidating far-field assumptions.

### 3.3 Non-Coherent Receivers with Multiple Antennas

A simple procedure for extending two antennas to multiple antennas is to apply the principles of Section 3.2 to any set of antenna pairs, such as using pairs of adjacent antennas, and averaging these individual angle estimates. Two more elaborated methods, employing the FFT or utilizing MuSiC, are presented in Section 4. Both are finally used within our system. Nevertheless, the following text contains some further information on quasi-coherent reception and arbitrary sending signals.

### 3.4 Quasi-Coherent Receivers

An approach to circumvent non-coherent operation is to employ a single receiving IC connected to multiple antennas by means of an antenna switch. That switch links one antenna after another to the IC, enabling quasi-coherent behavior. Thus, all down-converting and phase measurement are performed by the same local oscillator and reference, respectively. For that reason, all formulas in Section 3.1 remain applicable. A drawback is that phase drifts in any signal have a greater impact due to performing the measurements consecutively. An example is presented in the work of Sun and Karmakar [56] which operates on arbitrary periodic signals. It requires sophisticated synchronization to record equivalent parts of the signal at different signal periods. One such algorithm, Cyclic-MuSiC, is presented in Section 2. In any case, this approach is not applicable for non-periodic signals, since there is no relation between recordings conducted sequentially.

### 3.5 Arbitrary Sending Signals with Multiple Antennas

All approaches presented assume sending sinusoidal signals. In practice, however, it is desirable to use arbitrary waveforms, especially if the calculation of the angle of incidence is to be performed in parallel with the communication. For non-periodic signals, there is no time-independent relation in phase. Nevertheless, it is possible to generalize the preceding procedure by measuring the same signal received by different antennas and using cross correlation to determine the time difference with highest congruence, as proposed in the work of Tang [59] and Zinke [67]. Ideally, this time difference  $\Delta t$  characterizes the time it takes for the waves emitted by the sender to travel from receiving antenna 1 to receiving antenna 2. Employing Equation (3),  $\Delta d = c \cdot \Delta t$  and reordering yields the angle.

## 4 ALGORITHMS FOR DETERMINING THE AOA

In this section, two contrasting approaches to determining AoA are presented. FFT computation is very simple but often leads to performance degradation. The opposite is true for MuSiC, where improved accuracy is expected at the expense of computational cost.

### 4.1 FFT

The **Fourier Transform (FT)** as well as the z-transform (i.e., the basis for the discrete FT) are introduced in detail in the work of Marks [40]. The FFT is a specific implementation of the latter. On that account, the underlying mathematics is not recapitulated. Certainly, FT or FFT strip down a signal in the time domain, denoted as a complex number sequence ( $\underline{x}_r$ ) of size R, into its composed frequencies ( $\underline{X}_p$ ). Thus, a signal in the frequency domain is obtained by calculating

$$\underline{X}_p = \sum_{r=0}^{R-1} \underline{x}_r \exp\left(-i \frac{2\pi pr}{R}\right). \quad (16)$$

Assuming sinusoidal waves as before and performing the FFT, its amplitude spectrum ( $\underline{A}_p$ ) with

$$\underline{A}_p := |\underline{X}_p| \quad , \quad \forall p \in [0, R] \quad (17)$$

ideally contains one peak for every sending frequency. For any, the associated phase in the FFT comprises the information regarding the phase of the sinusoidal wave. Employing the differences of these phase results at any two adjacent antennas, one can determine the incident angle by applying Equations (10) or (15) for coherent or non-coherent reception, respectively. In the following, this approach is described in more detail for the latter.

Let  $\Delta\phi_{S \rightarrow \boxed{R_n}}$  be the particular phase difference from each of the N antennas, where  $n = 1, \dots, N$ . To eliminate  $\varphi_{\text{Offset}}$ , we refer all of these to the first antenna by specifying

$$\Delta\phi_{S \rightarrow \boxed{R_{1-n}}} := \Delta\phi_{S \rightarrow \boxed{R_n}} - \Delta\phi_{S \rightarrow \boxed{R_1}} \quad , \quad \forall n \in [2, N]. \quad (18)$$

For the sake of simplicity, we calculate the mean of these  $N - 1$  angles, denoted as  $\overline{\Delta\phi}_{S \rightarrow \boxed{R_{1-n}}}$ . The incident angle is now derived by utilizing (15) and substituting

$$\Delta\phi_{S \rightarrow \boxed{R_1}} - \Delta\phi_{S \rightarrow \boxed{R_2}} - \varphi_{\text{offset}} \rightarrow \overline{\Delta\phi}_{S \rightarrow \boxed{R_{1-n}}}. \quad (19)$$

### 4.2 MuSiC

The MuSiC algorithm [53], presented next, is one of the most used for determining the incident angle. Let the receiving node R be a ULA that is an arrangement of N antennas set up on a straight line with equal spacing  $a$ , denoted as  $R_1, \dots, R_N$  (see Figure 2). Furthermore, let there be M sending sources  $S_1, \dots, S_M$ , all located in the far-field of the receiving node, so that plane-wave characteristics can be assumed. In the following, we require  $N > M$ . Moreover, let there be no reflection and no multipath, and signal propagation shall only be toward **Line of Sight (LoS)**. Generalizing from pure sinusoidal (see Section 3) to modulated signals, the signal emitted from the  $m$ -th source ( $m \in 1, \dots, M$ )  $s_{\text{rf}, \boxed{S_m} \rightarrow R}(t)$  reads

$$s_{\text{rf}, \boxed{S_m} \rightarrow R}(t) = \hat{s}_{\text{rf}, \boxed{S_m}}(t) \cdot \sin\left(\omega_{\text{rf}, \boxed{S_m}} t + \varphi_{\text{rf}, \boxed{S_m}}\right). \quad (20)$$

Here,  $\hat{s}_{\text{rf}, \boxed{S_m}}(t)$  is its envelope and  $\omega_{\text{rf}, \boxed{S_m}} := 2\pi f_{\text{rf}, \boxed{S_m}}$ , where  $f_{\text{rf}, \boxed{S_m}}$  is the carrier frequency. As before, the received signal at antenna  $R_n$  ( $n \in 1, \dots, N$ ) can be written as

$$s_{\text{rf}, S_m \rightarrow \boxed{R_n}}(t) = \hat{s}_{\text{rf}, \boxed{S_m}}(t) \cdot \sin\left(\omega_{\text{rf}, \boxed{S_m}} \left[t - \frac{d_1}{c} - \frac{\Delta d_n}{c}\right] + \varphi_{\text{rf}, \boxed{S_m}}\right) \quad (21)$$

where, similar to Equation (3), it is valid

$$\Delta d_n = (n - 1) a \sin(\alpha_{\ll\bullet}). \quad (22)$$

Due to the size of the derivations for MuSiC, only the partial results necessary for further understanding are briefly summarized in the following. The complete derivation is provided in Appendix C.

First of all, the received signals from Equation (21) are considered in the frequency domain, where phasor transform is applied to have  $\underline{s}_{rf,S_m \rightarrow R_n}(t)$ . In an initial step, the signal matrix  $\tilde{\underline{s}}_{rf,R}(t_1, \dots, t_D)$  is computed by means of sampling at D different points in time  $t_1, \dots, t_D$ :

$$\tilde{\underline{s}}_{rf,R}(t_1, \dots, t_D) := \begin{pmatrix} \tilde{\underline{s}}_{rf,R_1}(t_1) & \tilde{\underline{s}}_{rf,R_1}(t_2) & \dots & \tilde{\underline{s}}_{rf,R_1}(t_D) \\ \vdots & \vdots & \ddots & \vdots \\ \tilde{\underline{s}}_{rf,R_N}(t_1) & \tilde{\underline{s}}_{rf,R_N}(t_2) & \dots & \tilde{\underline{s}}_{rf,R_N}(t_D) \end{pmatrix}. \quad (23)$$

Subsequently, the sampling covariance matrix  $E\widetilde{\text{COV}}\{\tilde{\underline{s}}_{rf,R}\}$  is derived, which reads

$$E\widetilde{\text{COV}}\{\tilde{\underline{s}}_{rf,R}\} := \frac{1}{N} \tilde{\underline{s}}_{rf,R}(t_1, \dots, t_D) \tilde{\underline{s}}_{rf,R}(t_1, \dots, t_D)^H. \quad (24)$$

It is proven in Appendix E that this matrix is Hermitian and of rank M. Of its N eigenvalues, M can be associated with the M signals and the remaining  $N - M$  with noise. The corresponding eigenvectors of the latter are concentrated within the following matrix:

$$V_{\text{Noise}} := \begin{pmatrix} \mathbf{v}_{M+1} & \mathbf{v}_{M+2} & \dots & \mathbf{v}_N \end{pmatrix}. \quad (25)$$

Last, a pseudo-spectrum  $P(\alpha_{\ll\bullet})$

$$P(\alpha_{\ll\bullet}) = \frac{1}{(V_{\text{Noise}}^H \underline{a}(\alpha_{\ll\bullet}) \underline{a}(\alpha_{\ll\bullet})^H V_{\text{Noise}})} \quad (26)$$

is set up, where the M highest peaks indicate the incident angles of the M sending sources. In the formula,  $\underline{a}(\alpha_{\ll\bullet})$  is the steering vector, defined as

$$\underline{a}(\alpha_{\ll\bullet}) := \left( 1 \quad \exp\left(-j\omega_{rf,S_m} \frac{\Delta d_2}{c}\right) \quad \dots \quad \exp\left(-j\omega_{rf,S_m} \frac{\Delta d_N}{c}\right) \right)^T. \quad (27)$$

## 5 ESTIMATING THE ANGLE FROM THE SPECTRUM

In the following, we present four variants to estimate the incident angle from the spectrum, where we limit ourselves to MuSiC. The first approach characterizes the conventional method. In contrast, the other three represent novel techniques with increasing complexity. To facilitate explanations, Figure 3 depicts four MuSiC spectra, which were recorded sequentially<sup>2,3</sup> at the same location with a true incident angle of 99.5° (actually these belong to BS 3 for measurement point 10 of our outdoor experiment from Section 9.2). We conclude with some remarks on the adaptation to the FFT.

<sup>2</sup>Sequential means that they were acquired one after the other without changing the scenario. Although the delay between the recordings was marginal, the spectra differ greatly in appearance. This indicates the potential for spectra-post-processing.

<sup>3</sup>The different appearance of the spectra is already caused by small amplitude variations of all signal paths including LoS and non-LoS (NLoS) propagation, as preliminary simulations reveal. Here, the amplitude variations in successive measurements are caused by additive noise as well as by pedestrians crossing the scene.

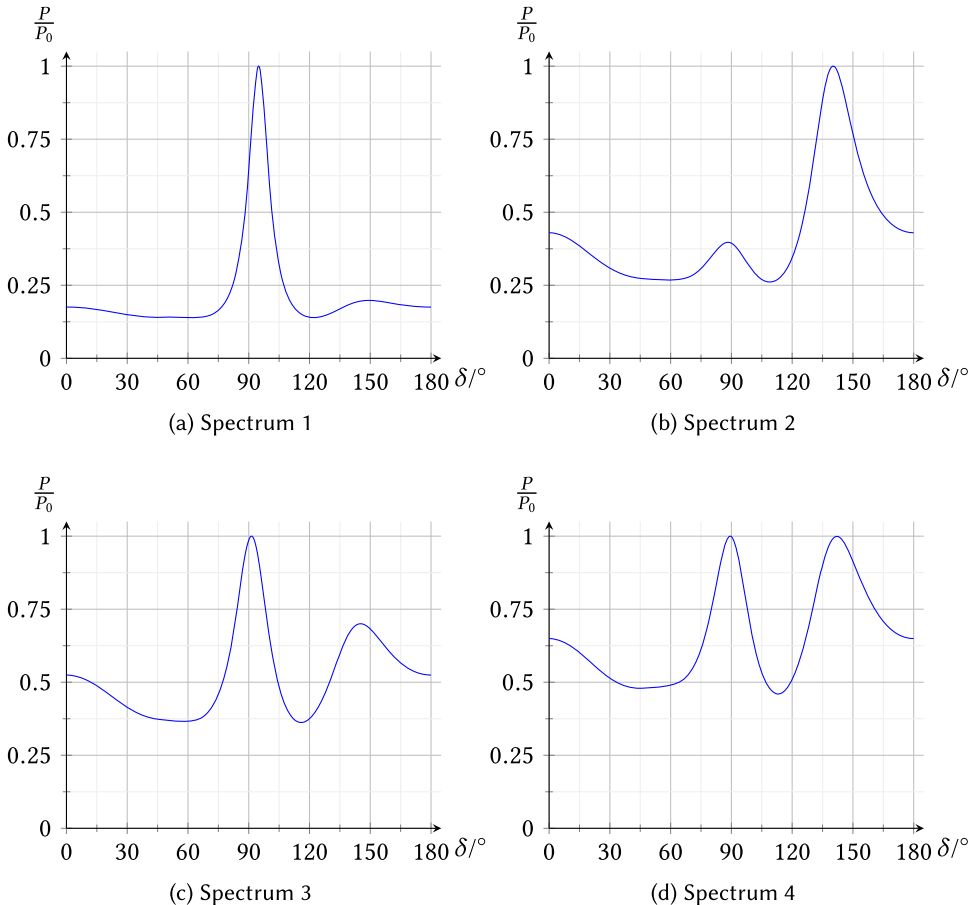


Fig. 3. MuSiC spectra examples belonging to BS 3 for measurement point 10 of our outdoor experiment from Section 9.2 (true angle:  $99.5^\circ$ ).

## 5.1 Searching Maximum

The solution most commonly used in the literature is to search for the maximum. The corresponding angle is used as the estimate. As can be seen, this gives an estimate close to the true value only for the first and the third spectrum in Figure 3. The result of the second spectrum is wrong and that of the fourth arbitrary. If only spectrum 2 is employed, it is not possible to derive an estimate that is close to the true value because one peak is higher than that for the direct path. However, if all these spectra are used together, it may be possible to derive a better estimate. In this context, we invent the following three alternatives, which all deal with multiple spectra.

## 5.2 Searching Maximum and Clustering

The first proposed approach is to search for the maximum in each spectrum, cluster these results, and select the mean of the longest cluster. More precisely, the maximum search is performed for each spectrum individually, whereas clustering uses these results from multiple spectra. In the preceding example, the maxima are at  $95.0^\circ$ ,  $140.2^\circ$ ,  $91.4^\circ$ , and  $89.4^\circ$ . Clustering is performed such that every result is first assigned to a single cluster (i.e., we have four clusters  $[95.0^\circ]$ ,  $[140.2^\circ]$ ,  $[91.4^\circ]$ , and  $[89.4^\circ]$ ). Then, we iteratively check whether two clusters can be merged. In this

context, two clusters are merged if the absolute difference of the means of the clusters is smaller than a certain threshold  $t_{\text{cluster}}$ . The value must be chosen such that peaks in different spectra that share the same angle of incidence of any propagation path are eventually merged into the same cluster. It must be a compromise to avoid that angles belonging to the same path are stored in different clusters if the value is too small, and that several different propagation paths are combined in one cluster if the value is too large. Therefore, we propose to estimate the variance of the angle measurements in advance and use a multiple of that value. In this context, we made some preliminary measurements in an indoor scenario where multipath effects are expected and examined the resulting spectra. We found that  $t_{\text{cluster}} := 10.0^\circ$  is a good compromise to use in this work. Clustering is terminated when no more merging is possible. In the example, we obtain the clusters  $[95.0^\circ, 91.4^\circ, 89.4^\circ]$  and  $[140.2^\circ]$ . The mean of the longest cluster, which is  $91.9^\circ$ , is returned as the estimate. Neither considering the shape of the maximum nor the remaining part of the spectrum is a drawback of this approach. A good spectrum is characterized by a single steep peak. In this regard, spectrum 1 is clearly superior to spectrum 4; however, both are receiving the same share in the cluster. The next two variants both take the shape of the spectrum into account.

### 5.3 Searching Peaks, Calculating Area, and Weighted Clustering

To mitigate the preceding drawback, we propose to relate the area under a peak to the total area under the plot. Before explaining the algorithm, we need to define the prominence of a peak. It was initially invented in the work of Helman [24] to describe mountain peaks as the height of a mountain above the saddle on the highest ridge connecting it to an even higher peak. However, it is also meaningful for describing spectral peaks. To determine the prominence of some peak, a horizontal line is drawn from the maximum value of that peak to the left and right until it either hits the border of the domain or the signal again. This horizontal line defines an interval in which the minimum points to the left and right of the peak are then searched, called *base points*. The prominence is defined as the vertical difference between the higher base point and the peak.

In a first step, each spectrum is again examined individually. Here, we look for all peaks in the spectrum whose prominence is above a certain threshold  $t_{\text{prominence}}$ , to disregard minor peaks. For each of the remaining, we calculate the corresponding area under each peak. To simplify the explanations, we use  $t_{\text{prominence}} := 0.1$  in this section.<sup>4</sup> Let  $x_{\text{peak}}$  be the x-coordinate (i.e., the angle) of the maximum of some peak. The associated area is determined as the area under the plot in the interval  $[x_{\text{peak}} - t_{\text{peak}}, x_{\text{peak}} + t_{\text{peak}}]$ , where  $t_{\text{peak}}$  is a configurable parameter for the interval width, which should be small. The reason for this is that compared to flat peaks, steep peaks tend to have its area close to the peak, and therefore steep peaks should be given a larger associated area. Finally, for each peak, we relate that area to the total area under the graph, which we call *area ratio*. We found that  $t_{\text{peak}} := 3.6^\circ$  is a good compromise, which will be used throughout this work.<sup>5</sup> For the first spectrum of the example from the last section, we obtain  $[(95.0^\circ, 0.08)]$ . Here, the tuples  $(\cdot)$  denote aggregations of the angle of a peak (here:  $95.0^\circ$ ) and the corresponding area ratio (here: 0.08). Similarly, we get  $[(140.2^\circ, 0.04), (88.4^\circ, 0.02)]$  for spectrum 2,  $[(145.2^\circ, 0.03), (91.4^\circ, 0.04)]$  for spectrum 3, and  $[(142.2^\circ, 0.03), (89.4^\circ, 0.03)]$  for spectrum 4.

In a second step, we use these results from multiple spectra together to perform clustering similarly to before. The following clusters are obtained:

- $[(95.0^\circ, 0.08), (88.4^\circ, 0.02), (91.4^\circ, 0.04), (89.4^\circ, 0.03)]$ ,
- $[(140.2^\circ, 0.04), (145.2^\circ, 0.03), (142.2^\circ, 0.03)]$ .

<sup>4</sup>This value is only used for explanation purposes: it ensures that all peaks visible in Figure 3 are recognized by the algorithm.

<sup>5</sup>To determine that number, preliminary measurements were performed.

We sum the area ratio of each cluster and select the one with maximum (here, 0.17 for the first cluster). Finally, the weighted average of all incident angles  $\tilde{\alpha}_{\triangleleft\bullet,i}$  of this cluster is calculated using the area ratio as weights  $w_i$ —that is,

$${}^E\tilde{\alpha}_{\triangleleft\bullet} := \frac{\sum_{i=1}^I w_i \cdot \tilde{\alpha}_{\triangleleft\bullet,i}}{\sum_{i=1}^I w_i} \quad (28)$$

where  $I$  is the size of the cluster. For the example, we have

$${}^E\tilde{\alpha}_{\triangleleft\bullet} = \frac{95.0^\circ \cdot 0.08 + 88.4^\circ \cdot 0.02 + 91.4^\circ \cdot 0.04 + 89.4^\circ \cdot 0.03}{0.08 + 0.02 + 0.04 + 0.03} = 92.4^\circ.$$

Please note that even though the weights tend to be very small, only their relation to each other is considered in Equation (28).

#### 5.4 Searching Peaks, Calculating Relevance, and Weighted Clustering

The final approach we propose is similar to the last one, except that we no longer measure area. Instead, we define relevance as a new metric, which is composed of some measure for the height and for the width of a peak, as explained in the following. In the last method, prominence was only used to detect meaningful peaks. Here, we include it more directly to define the height-based quality  $Q_{h,i}$  for the  $i$ -th peak in the spectrum as

$$Q_{h,i} := \exp\left(p_i - \sum_{\substack{k=1 \\ k \neq i}}^K p_k\right) \quad (29)$$

where the prominences  $p_k$  of all  $K$  peaks in that same spectrum are utilized. Using the exponential function ensures that the height-based quality for a peak increases with increasing prominence. However, high values can be obtained by subtracting the other prominences only if there are few insignificant other peaks.

Additionally, a width-based quality  $Q_{w,i}$  for the  $i$ -th peak is set up as follows:

$$Q_{w,i} := \frac{t_{width}}{b_i}. \quad (30)$$

Here,  $t_{width}$  is a configurable parameter to limit the range of this measure and  $b_i$  characterizes the width of the peak. The latter is calculated by finding the nearest point to the right and left of the peak, respectively, where the value has decreased to the mean between the associated base point value and the peak value. Thus, we intend to measure the width at these points, where the peak has decreased by 50%. We found that  $t_{width} := 9^\circ$  is a good compromise,<sup>6</sup> to use throughout the article. Finally, the relevance for the  $i$ -th peak reads

$$R_i := Q_{h,i} \cdot Q_{w,i}. \quad (31)$$

Considering the last example again, let there be the following prominences and widths:

- Spectrum 1: peak at  $95.0^\circ \rightarrow p_1 = 0.86, b_1 = 11.4^\circ$
- Spectrum 2: peak at  $140.2^\circ \rightarrow p_1 = 0.57, b_1 = 20.5^\circ$  and peak at  $88.4^\circ \rightarrow p_2 = 0.13, b_2 = 18.8^\circ$
- Spectrum 3: peak at  $145.2^\circ \rightarrow p_1 = 0.18, b_1 = 22.5^\circ$  and peak at  $91.4^\circ \rightarrow p_2 = 0.63, b_2 = 16.9^\circ$
- Spectrum 4: peak at  $142.2^\circ \rightarrow p_1 = 0.35, b_1 = 22.9^\circ$  and peak at  $89.4^\circ \rightarrow p_2 = 0.52, b_2 = 18.3^\circ$ .

<sup>6</sup>To determine that number, preliminary measurements were performed.

Thus, we have  $Q_{h:1} = \exp(0.86) = 2.36$ ,  $Q_{w:1} = 0.79$ , and finally  $R_1 = 1.86$  for spectrum 1. Briefly, we write  $[(95.0^\circ, 1.86)]$ , using some similar notation as before. Likewise, we obtain for

- Spectrum 2:  $[(140.2^\circ, 0.68), (88.4^\circ, 0.31)]$ ,
- Spectrum 3:  $[(145.2^\circ, 0.26), (91.4^\circ, 0.84)]$ , and
- Spectrum 4:  $[(142.2^\circ, 0.33), (89.4^\circ, 0.58)]$ .

Employing weighted clustering as in the last paragraph and utilizing Equation (28) again, the estimated incident angle reads  ${}^E\tilde{\alpha}_{\triangleleft\bullet} = 92.7^\circ$ .

Investigations into the necessary cluster size  $I$  for the preceding methods are beyond the scope of this work, as it certainly depends on the underlying environment. For example, in a scenario without multipath propagation, a small sample is certainly sufficient, whereas under **Non-Line of Sight (NLoS)** conditions a larger number is beneficial. These statistical studies should be performed for a wide range of environments, which we plan to do in future work.

## 5.5 Adaptation to the FFT

For each individual measurement, MuSiC generates a spectrum that contains the information of all antennas, whereas the FFT generates a spectrum for each antenna. In this regard, the first two approaches, which deal with finding the maximum with and without clustering, can be easily adapted to the FFT by applying the techniques to the individual antenna spectra. To support the other two approaches as well, we would first need to develop means of combining these individual FFT spectra from each antenna, which is beyond the scope of this work.

## 6 POSITIONING

Until now, we performed measurements of the incident angle at one BS, where a signal was emitted from the MS, whose position and thus true incident angle is unknown. To derive the position of that MS, we need to extend that procedure to multiple BS measuring this signal in parallel so that a position as the intersection of these incident angles can be estimated. In the following, we introduce two related positioning techniques from the literature, where the former equally deploys multiple angle measurements. In contrast, the latter applies some rating of these results by incorporating weights.

### 6.1 Simple Iterative

The iterative approach minimizes the sum of squared errors  $\varepsilon$  of the estimated incident angles at multiple BS. Let  $(x_n, y_n)^T$  be the position of BS  $n$  ( $n = 1, \dots, N$ ) and let  $(x, y)^T$  be the sought unknown position of the MS, then the error reads

$$\tilde{\varepsilon} = \sum_{n=1}^N \underbrace{\left[ \tan^{-1} \left( \frac{y - y_n}{x - x_n} \right) - \tilde{\alpha}_{\triangleleft n, \bullet} \right]}_{\alpha_{\triangleleft n, \bullet}}^2. \quad (32)$$

Here,  $\tilde{\alpha}_{\triangleleft n, \bullet}$  characterizes the estimated incident angle to the MS at BS  $n$ . The unknown position is derived via gradient descent—that is,

$$\begin{pmatrix} {}^E\tilde{x} \\ {}^E\tilde{y} \end{pmatrix}_{k+1} = \begin{pmatrix} {}^E\tilde{x} \\ {}^E\tilde{y} \end{pmatrix}_k - \alpha \begin{pmatrix} \frac{d\tilde{\varepsilon}}{dx} \\ \frac{d\tilde{\varepsilon}}{dy} \end{pmatrix}_{x={}^E\tilde{x}_k, y={}^E\tilde{y}_k} \quad (33)$$

where  $\alpha$  is the step size [60]. A disadvantage of this approach is that convergence is not always guaranteed. For that reason, we propose to discretize the underlying scenario and evaluate

Equation (32) at each possible location. The estimated position is the one with minimum value. We refer to this technique as simple iterative. Certainly, the goal is to have the grid as dense as possible, depending on computing power. In the following course of the article, we chose the distance between two adjacent discretization points to be 0.05 m.

## 6.2 Simple Weighted Iterative

Building on this, we now include weights. Therefore, we first consider the individual error, which is

$$\tilde{\varepsilon}_n = \left[ \underbrace{\tan^{-1} \left( \frac{y - y_n}{x - x_n} \right)}_{\alpha_{\triangle n, \bullet}} - \tilde{\alpha}_{\triangle n, \bullet} \right]^2. \quad (34)$$

The total error according to [37, 60] is given as

$$\tilde{\varepsilon} = \tilde{\varepsilon}^T S^{-1} \tilde{\varepsilon}, \text{ with } \tilde{\varepsilon}^T = (\tilde{\varepsilon}_1 \quad \tilde{\varepsilon}_2 \quad \dots \quad \tilde{\varepsilon}_N)^T \quad (35)$$

where  $S$  characterizes the covariance error matrix. For simplicity, we assume that the errors are independent random variables. Hence, the covariance matrix is diagonal—that is,

$$S = \begin{pmatrix} \text{Var}\{\tilde{\varepsilon}_1\} & 0 & \dots & 0 \\ 0 & \text{Var}\{\tilde{\varepsilon}_2\} & \dots & 0 \\ \vdots & \vdots & \ddots & \vdots \\ 0 & 0 & \dots & \text{Var}\{\tilde{\varepsilon}_N\} \end{pmatrix}. \quad (36)$$

According to Appendix G, we have for the variance

$$\begin{aligned} \text{Var}\{\tilde{\varepsilon}_n\} &= 4\alpha_{\triangle n, \bullet}^2 \left( \mathbb{E}\{\tilde{\alpha}_{\triangle n, \bullet}^2\} - \mathbb{E}\{\tilde{\alpha}_{\triangle n, \bullet}\}^2 \right) + \left( \mathbb{E}\{\tilde{\alpha}_{\triangle n, \bullet}^4\} - \mathbb{E}\{\tilde{\alpha}_{\triangle n, \bullet}^2\}^2 \right) \\ &\quad - 2\alpha_{\triangle n, \bullet} \left( \mathbb{E}\{\tilde{\alpha}_{\triangle n, \bullet}^3\} - \mathbb{E}\{\tilde{\alpha}_{\triangle n, \bullet}\} \mathbb{E}\{\tilde{\alpha}_{\triangle n, \bullet}^2\} \right). \end{aligned} \quad (37)$$

The total error now reads

$$\tilde{\varepsilon} = \tilde{\varepsilon}^T S^{-1} \tilde{\varepsilon} = \sum_{n=1}^N \frac{\tilde{\varepsilon}_n^2}{\text{Var}\{\tilde{\varepsilon}_n\}}. \quad (38)$$

If the measurements of the incident angles are additionally Gaussian distributed according to

$$\tilde{\alpha}_{\triangle n, \bullet} \sim \mathcal{N}(\alpha_{\triangle n, \bullet}, \sigma_{\triangle n, \bullet}^2), \quad (39)$$

then this simplifies to

$$\text{Var}\{\tilde{\varepsilon}_n\} = 2\sigma_{\triangle n, \bullet}^4 \quad (40)$$

according to Equation (77) in Appendix G.

The remaining steps are identical to before—that is, we iteratively perform Equation (33). Again, we avoid the convergence problem by discretizing the scenario. We refer to this as simple weighted iterative.

We are not aware of the variances of the angle measurements, especially in the case of strong multipath. However, in our approaches from Sections 5.3 and 5.4, we derived some similar metrics (i.e., area ratio and relevance). For each of these two algorithms, we propose to use these measures instead of the variance in Equation (40) for this positioning technique. To be more precise, we substitute  $\sigma_{\triangle n, \bullet} \rightarrow w_n$  and  $\sigma_{\triangle n, \bullet} \rightarrow R_n$  for the approaches based on the area ratio and relevance, respectively.

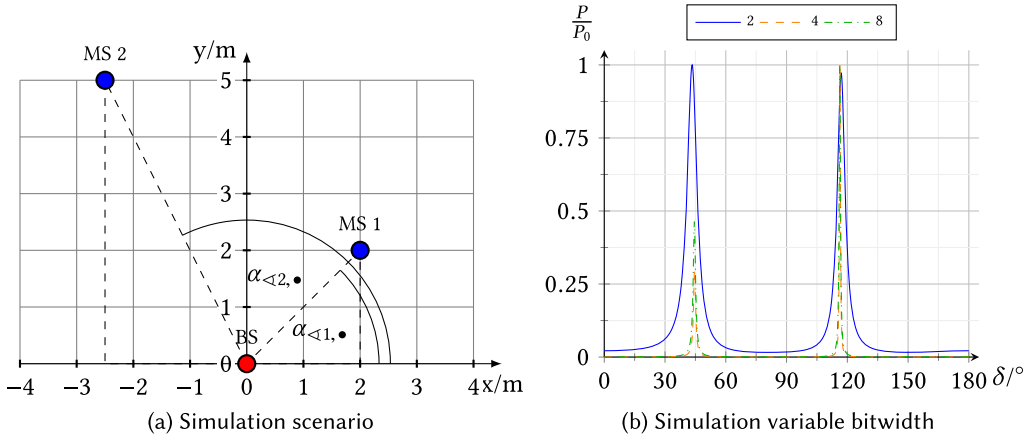


Fig. 4. Simulation scenario and simulation variable bitwidth.

## 7 SIMULATIONS

This paragraph is intended as explorative work to fix the specifications for our system. The ultimate goal is to use the two approaches discussed in Section 4 (i.e., both FFT and MuSiC). Since the final results by MuSiC are assumed to be superior under optimal conditions, we focus our investigations on MuSiC in the following. Therefore, we first perform simulations on optimal sampling parameters. Later, we analyze the influence of variable phase angles for non-coherent behavior and explore misalignments during sampling. Considerations on antenna spacing are deferred until Appendix A.

Throughout the simulations, we assume two uncorrelated sending sources at incident angles of  $45.0^\circ$  and  $116.5^\circ$ , respectively, as shown in Figure 4(a).<sup>7</sup> Similar to our hardware presented in the subsequent section, the transmission is to be at 2.4 GHz, with the down-converted signals at 100 kHz and 105 kHz,<sup>8</sup> respectively. The spacing between the four antennas is approximately half the wavelength (i.e.,  $a = 6$  cm). Certainly, a higher antenna count is advantageous. However, due to the goal to accommodating them on a **Printed Circuit Board (PCB)**, we limit ourselves to four.

### 7.1 Sampling Rate, Bitwidth, and Number of Samples

In the following, we characterize the effects of sampling rate, bitwidth, and number of samples on the MuSiC spectrum. To include noise, we add **Additive White Gaussian Noise (AWGN)** with SNR = 30 dB<sup>9</sup> at each receiving antenna.<sup>10</sup>

**7.1.1 Bitwidth.** Figure 4(b) shows three spectra where 100 samples are recorded with a sampling rate of 1 MHz. The bitwidth of the samples is 2, 4, and 8, respectively. It can be seen that as the bitwidth increases, the peaks become sharper and move toward the correct angles of incidence.

**7.1.2 Sampling Rate and Number of Samples.** Two spectra sampled with 250 kHz and 1 MHz are visualized in Figure 5(a), each with 10 samples recorded. In contrast, Figure 5(b) uses

<sup>7</sup>Again we assume plane-wave behavior at the receiving antennas.

<sup>8</sup>To be more precise, the associated transmit signals at 2.4 GHz must differ by 5 kHz according to Equation (6).

<sup>9</sup>This value was determined by some preliminary measurements of our real hardware from Section 8.

<sup>10</sup>The two sending sources in Figure 4(a) differ in terms of range to the receiver. Considering the path losses, the influence of AWGN on the received signal of the more distant source may prevail. In the following, however, we are not interested in comparing the results of both sources in the spectrum but in obtaining both peak values simultaneously as well as possible.

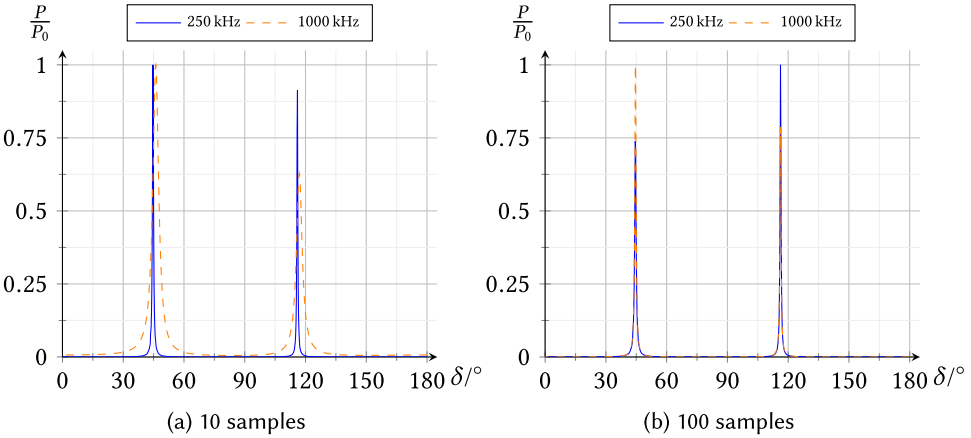


Fig. 5. Simulation of variable sampling rate and number of samples for sinusoidal signals.

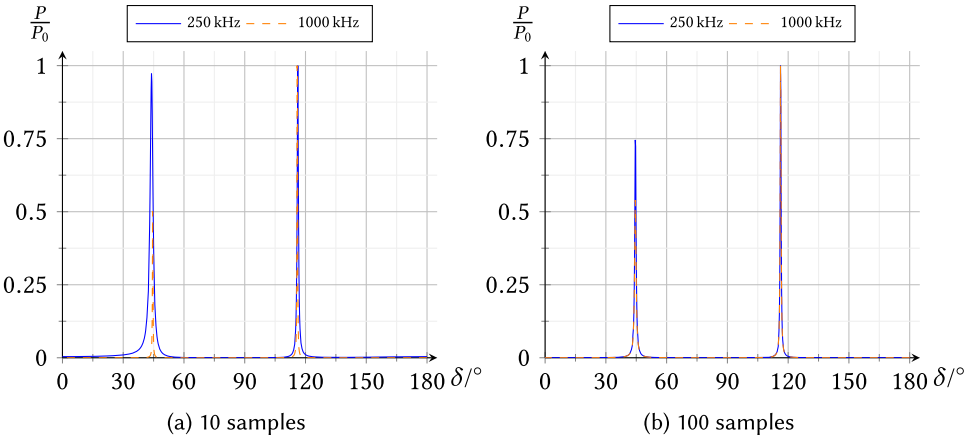


Fig. 6. Simulation of variable sampling rate and number of samples for Gaussian noise.

100 samples.<sup>11</sup> In the first case, a lower sampling rate results in a better spectrum; in the second case, this statement is not true. It can be concluded that neither the sampling rate nor the number of samples alone have influence on the result. Rather, the number of signal periods recorded seems to affect the spectrum. For periodic signals and a small number of samples, a lower sampling rate is beneficial because more signal periods are recorded. In contrast, Figure 6(a) shows sampling of AWGN at 250 kHz and 1 MHz for 10 samples. Here, a higher sampling rate results in sharper maxima, showing that the preceding statement is only true for periodic signals. With a higher number of samples, the difference disappears according to Figure 6(b).

## 7.2 Variable Phase Angles After Down-Mixing

Next, we investigate non-vanishing phase offsets  $\phi_{\text{offset}}$  between adjacent antennas that occur in the case of non-coherent reception (see Equation (15)). We choose 1,000 samples and a sampling rate of 1 MHz. All other parameters are kept as before. Figure 7(a) illustrates the results for different

<sup>11</sup>We are interested in the general trend regarding the influence of sampling rate and number of samples on the MuSiC spectrum. The concretely chosen parameters are therefore only illustrative.

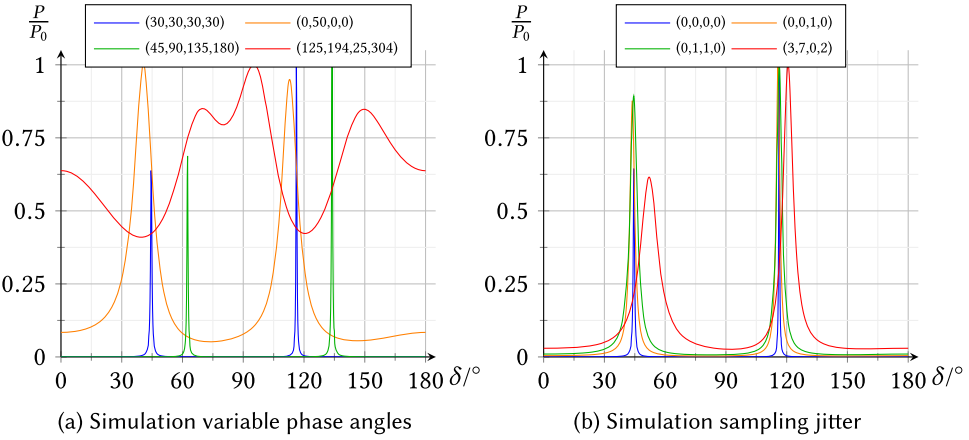


Fig. 7. Simulation variable phase angles and sampling jitter.

phase offsets. The four values in the legend for each plot denote the additive phase values after down-mixing and comparison with a reference—that is, the sum of the second through fifth terms in Equation (13). Thus, the blue plot is the ideal coherent result. As expected, only in this case, the MuSiC spectrum is of high quality. The orange plot highlights the case where there is an uncompensated phase offset. This results in a shift and broadening of the peaks, the former leading to systematic errors and the latter to random errors for the actual angles of incidence. Linearly increasing phase offsets (green plot) only cause a shift of the graph. Random phase offsets (red plot) produce a random output, which only allows the identification of the number of the signal sources but not the incident angles. This supports our statements in Section 3 to compensate non-coherent behavior by calibration.

### 7.3 Misaligned Sampling

Figure 7(b) shows the consequences of jitter when sampling between the antennas. Again, the blue plot depicts the ideal case with two sharp peaks at the correct angles of incidence. In contrast, for the orange plot, the sampling at the third antenna is delayed by only one sample, which already results in broadening and shifting of the peaks. These effects intensify if the second antenna is also late by one sample (green plot) and worsen with even greater jitter (red plot).

### 7.4 System Design Conclusions

In the following, we draw conclusions from the preceding simulations to refine the system design specification. In Section 7.1, it was shown that larger bitwidths as well as a larger number of samples are associated with better accuracy. For periodic signals, a higher sampling rate improves accuracy only if enough signal periods are recorded. In contrast, non-periodic signals benefit directly from higher sampling rates. Therefore, the sampling rate must be configurable. As has been shown, reasonable values for down-converted sending signals around 100 kHz are 8 bit bitwidth, 1 MHz sampling rate, and at least 100 sampling points at each antenna. Section 7.2 emphasizes that the phase offset  $\varphi_{\text{offset}}$  (see Equation (15)) must vanish. This can be done either by using coherent receivers (see Section 3.1) or by calibration (see Section 3.2). For MuSiC, the latter may be achieved by utilizing a calibration signal at a known position, determining the differences in the initial phase offsets at each adjacent receiving antenna, such as by running the FFT. These are then incorporated into the steering vector by shifting each phase by the differences of the initial phases. Section 7.3 shows that measurements on all receiving antennas must be performed in a synchronized manner.

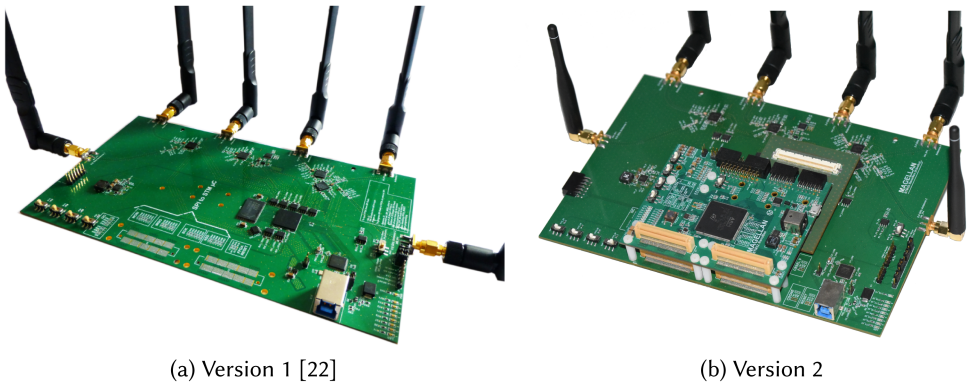


Fig. 8. Photos of the PCB modules.

Even an offset of one sample degrades the spectrum considerably. Misalignment is eliminated if the sampling jitter between the antennas is significantly less than the sampling frequency, since sampling then refers to approximately the same point in time. Thus, the jitter must be as low as possible.

## 8 DESIGN OF THE SYSTEM

To prove the concept for our AoA-based secondary RADAR positioning system, hardware, firmware, and software are implemented as described in the following sections. For the hardware, some information has already been published in previous work [22].

### 8.1 Hardware Design

In the following, we present our PCB modules as shown in Figure 8. These modules are used for the BS, the calibrator, and the cooperative MS. For determining the incident angle, we placed four antennas on the long back side, each controlled by a single RF transceiver at 2.4 GHz. Here, we employ the commercial Atmel AT86RF215 RF transceiver. On each transverse side is an additional antenna for 0.9-GHz communication, driven by the first and fourth ICs, respectively. A Lattice iCE40HX8K **Field Programmable Gate Array (FPGA)** is responsible for parallel configuration of the RF transceiver and either sends the results to a host PC via **Universal Serial Bus (USB)** 3.0 (version 1) or stores them in static random access memory (version 2). We made sure that the distance between the USB units and the 2.4-GHz nets is as far apart as possible to avoid coupling between these high-frequency nets. For configuration and debugging purposes, we added five switches, eight light-emitting diodes, and an 8-pin general-purpose input/output header. The FPGA configuration can be loaded either via a **Serial Peripheral Interface (SPI)**, from a separate flash memory, or via a programming interface. Our first version is intended as a stand-alone solution, where everything is configured via USB from a host. However, the second version is already included within our hybrid positioning system [19, 21], via two 100-pin connectors on the front side. These are left empty in the first version. The second version is controlled by our data processing PCB with an ST microcontroller STM32F7 or STM32H7 stacked on the long front side (for more information, see previous work [19]). Nevertheless, both versions are almost identical. The main reason for implementing another PCB was the poor solder yield for the ball grid array FPGA on this large PCB so that the FPGA was offloaded to a small, separate stacked PCB. We also added extra IRQ signals for use in our hybrid positioning system. In both cases, the PCB is powered by **5-V Direct Current (DC)**, either via USB or the 100-pin connectors. Voltage conversion to 3.3 V, 2.5 V, and 1.2 V for the FPGA is implemented using DC-DC converters, which are also placed far

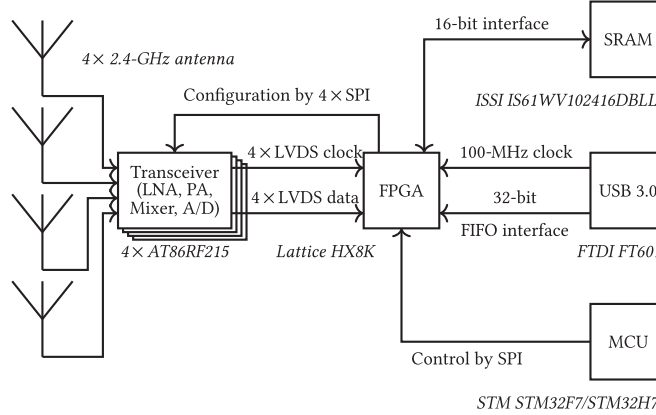


Fig. 9. Block diagram of modules for the BS, calibrator, and cooperative MS target.

away from high-frequency nets. In Appendix A, three important additional design parameters (i.e., antenna spacing, antenna characteristics, and clock generation) are examined in more detail.

## 8.2 Firmware Design

Figure 9 presents the block diagram of the modules used for the BS, the calibrator, and the cooperative MS at the unknown position. The four single-ended 2.4-GHz antennas are connected to the differential inputs at the transceiver ICs via baluns. In receive mode, this chip [3] amplifies these signals by means of a **Low Noise Amplifier (LNA)** and down-converts it to an intermediate frequency in the range of 320 to 2,500 kHz. These signals are then sampled in an analog-to-digital converter at a fixed rate of 32 MHz, with this rate later reduced to 4 MHz by down-sampling. Additionally, this signal is converted to zero-IF. Depending on the configuration, the signal can be further down-sampled to achieve a final rate between 400 kHz and 4,000 kHz. This serial I/Q-data stream is output via a **Low-Voltage Differential Signaling (LVDS)** interface, with real and imaginary values encoded as 13-bit integers.<sup>12</sup> Both are bundled into a 32-bit word, with the remaining 6 bits used for synchronization. Thus, at a sampling rate of 4 MHz, there are up to 128 Mbit/s of LVDS data. In any case, the LVDS clock is 64 MHz, with the rising and falling edge indicating a new bit. For reduced sampling rates, some 32-bit LVDS words are kept empty [3].

The FPGA is responsible for synchronization, decoding, and buffering each of these four individual LVDS streams. A combined multiplexed stream is then generated. As mentioned earlier, it is either sent to a host PC via USB 3.0 or stored in static random access memory for subsequent retrieval by a **Micro-Controller Unit (MCU)** via SPI. The digital logic in the FPGA operates at 32 MHz, so along with the LVDS clock, five clock domains must be processed by the FPGA. The transceiver ICs are configured via the SPI by the FPGA, which in turn receives its commands from the host PC or the MCU.

## 8.3 Software Design

We implement the software for our first version as a Python framework running on a host PC, which reads the I/Q-data via USB 3.0 and calculates the FFT and MuSiC estimates as described in the following. In contrast, the software for our second version is implemented in C++ and runs on

<sup>12</sup>The 13-bit integers are larger than the required minimum value of 8-bits derived in Sections 7.1 and 7.4.

---

**ALGORITHM 1:** FFT

**Require:** I/Q-data for calibration and measurement.

- 1: Calculate signal matrix  $\tilde{S}_{\text{rf}, \text{Cal}}(t_1, \dots, t_D)$  according to Equation (23) from calibration data.
  - 2: Initialize a calibration phase vector  $\Delta\varphi_{\text{Cal}} = [0, \dots, 0]$ .
  - 3: **for** each row  $\tilde{s}$  in  $\tilde{S}_{\text{rf}, \text{Cal}}(t_1, \dots, t_D)$  **do**
  - 4:     Calculate the FFT  $\tilde{\mathcal{F}}(\tilde{s})$ .
  - 5:     Find maximum and determine associated phase  $\varphi$ .
  - 6:     Set element of current row index in  $\Delta\varphi_{\text{Cal}}$  to  $\varphi$ .
  - 7: **end for**
  - 8: Relate all to first IC  $\Delta\varphi_{\text{Cal}} := \Delta\varphi_{\text{Cal}} - \Delta\varphi_{\text{Cal}}[0]$ .
  - 9:
  - 10: Calculate signal matrix  $\tilde{S}_{\text{rf}, \text{Mes}}(t_1, \dots, t_D)$  according to Equation (23) from measurement data.
  - 11: Initialize a measurement phase vector  $\Delta\varphi_{\text{Mes}} = [0, \dots, 0]$ .
  - 12: **for** each row  $\tilde{s}$  in  $\tilde{S}_{\text{rf}, \text{Mes}}(t_1, \dots, t_D)$  **do**
  - 13:     Calculate the FFT  $\tilde{\mathcal{F}}(\tilde{s})$ .
  - 14:     Find the M highest peaks for the M incident angles and determine the associated phases  $\varphi_1, \varphi_2, \dots, \varphi_M$  (sorted in increasing order) in the interval  $[0, 2\pi]$ .
  - 15:     Set up row vector  $\varphi := (\varphi_1, \varphi_2, \dots, \varphi_M)$ .
  - 16:     Set row vector with current row index in  $\Delta\varphi_{\text{Mes}}$  to  $\varphi$ .
  - 17: **end for**
  - 18: Relate all to first IC  $\Delta\varphi_{\text{Mes}} := \Delta\varphi_{\text{Mes}} - \Delta\varphi_{\text{Mes}}[0]$ .
  - 19:
  - 20: Determine  $\Delta\varphi[i] := \Delta\varphi_{\text{Cal}} - \Delta\varphi_{\text{Mes}}[i]$  for  $\forall i \in [1, M]$ .
  - 21: Normalize all angles to be within  $[0, 2\pi]$ .
  - 22: Calculate M incident angles as mean of all coordinates of all M row vectors in  $\Delta\varphi$ .
- 

the STM32F7/STM32H7 MCU. In both cases, the pseudo-code for the FFT is outlined in Algorithm 1 and for MuSiC in Algorithm 2.

Several comments are in order. As explained before, there is an initial phase offset  $\varphi_{\text{offset}}$  according to Equation (15) between adjacent transceiver IC,<sup>13</sup> which must be compensated before determining the incident angle. For this reason, we use a two-stage procedure. In the first step, a calibrator station at a known position sends a sinusoidal wave, where the I/Q-data at all receiving transceiver ICs are recorded. We refer to this data as calibration data. In both algorithms, we compensate for these offsets by utilizing the FFT (lines 1–8). The second step is the actual measurement, where the MS at the unknown position transmits a sinusoidal wave. This data (this time denoted as measurement I/Q-data) is also recorded by the BS. In Algorithm 1, we perform the same steps for the measurement data as for the calibration data. In contrast, in Algorithm 2, MuSiC is used. Here, any algorithm from Section 5 can be used as the last step (line 17). Although we express both algorithms for arbitrary  $M \geq 1$ , in our implementations we only use  $M = 1$ . This is justified since we are only looking for the position of a single MS. In other words, only this one MS sends its reference signal. After several measurements are taken at each BS, the positioning algorithms from Section 6 are then employed.

The most challenging step in MuSiC is the computation of the eigenvalues and eigenvectors. In our first version, we simply use the Python `numpy.linalg` package. In contrast, in our second

<sup>13</sup>These phase offsets are caused by small differences in length of the connecting lines between the crystal and the individual ICs, which result in small phase differences at the input of the ICs for this clock signal. Internally in the ICs, that signal is attached to a PLL to consequently generate multiple high-frequency signals, such as the local oscillator signals. Due to up-conversion, these small phase differences lead to enormous phase differences at high frequencies.

---

**ALGORITHM 2:** MuSiC

---

**Require:** I/Q-data for calibration and measurement.

- 1: Calculate signal matrix  $\tilde{s}_{\text{rf[R]Cal}}(t_1, \dots, t_D)$  according to Equation (23) from calibration data.
  - 2: Initialize a calibration phase vector  $\Delta\varphi_{\text{Cal}} = [0, \dots, 0]$ .
  - 3: **for** each row  $\tilde{s}$  in  $\tilde{s}_{\text{rf[R]Cal}}(t_1, \dots, t_D)$  **do**
  - 4:     Calculate the FFT  $\tilde{\mathcal{F}}(\tilde{s})$ .
  - 5:     Find maximum and determine associated phase  $\varphi$ .
  - 6:     Set element of current row index in  $\Delta\varphi_{\text{Cal}}$  to  $\varphi$ .
  - 7: **end for**
  - 8: Relate all to first IC  $\Delta\varphi_{\text{Cal}} := \Delta\varphi_{\text{Cal}} - \Delta\varphi_{\text{Cal}}[0]$ .
  - 9:
  - 10: Calculate signal matrix  $\tilde{s}_{\text{rf[R]Mes}}(t_1, \dots, t_D)$  according to Equation (23) from measurement data.
  - 11: Calculate measurement covariance matrix  $E\widetilde{\text{COV}}\{\tilde{s}_{\text{rf[R]}}\}$  according to Equation (24).
  - 12: Calculate eigenvalues and eigenvectors of  $E\widetilde{\text{COV}}\{\tilde{s}_{\text{rf[R]}}\}$ .
  - 13: Sort eigenvalues so that  $\lambda_1 > \dots > \lambda_M > \lambda_{M+1} > \lambda_N$ .
  - 14: Utilize associated eigenvectors  $v_{M+1}, \dots, v_N$  in  $V_{\text{Noise}}$  according to Equation (25).
  - 15: Calculate steering vectors  $a(\alpha_{\triangleleft\bullet})$  according to Equation (27) for any desired selection of  $\alpha_{\triangleleft\bullet}$ .
  - 16: Calculate pseudo-spectrum  $P(\alpha_{\triangleleft\bullet})$  according to Equation (26) for all steering vectors selected.
  - 17: Determine M incident angles according to the algorithms in Section 5.
- 

version, we implement such an approach, namely the QR-algorithm based on iterative QR-decomposition presented in the work of Lawson and Hanson [35], in C++ for the embedded MCU.

## 9 EXPERIMENTS

To prove our AoA-based secondary RADAR positioning concept described in the previous sections, we perform experimental measurements in two different scenarios. These are an outdoor open space courtyard and a university indoor hall. As mentioned in Section 8, the system is specifically tailored for MuSiC. The reason for the additional presentation of the FFT results is twofold. First, we want to show that our developments are not only limited to MuSiC. Second, we provide these results for comparison. This section also includes some comments on energy consumption.

In the following, we consider the mean position error across all L measurement locations as the average of the individual absolute errors as

$$\text{Mean positioning error: } \frac{1}{L} \sum_{l=1}^L \sqrt{(\tilde{x}_l - x_l)^2 + (\tilde{y}_l - y_l)^2} \quad (41)$$

where  $(\tilde{x}_l, \tilde{y}_l)^T$  is the position estimate for the l-th measurement with true position  $(x_l, y_l)^T$ . Similarly, the mean angle error over all N BS and all L measurement locations is defined as

$$\text{Mean angle error: } \frac{1}{L} \sum_{l=1}^L \left( \frac{1}{N} \sum_{n=1}^N \sqrt{(\tilde{\alpha}_{\triangleleft n, \bullet l} - \alpha_{\triangleleft n, \bullet l})^2} \right) \quad (42)$$

where  $\tilde{\alpha}_{\triangleleft n, \bullet l}$  is the angle estimate for the l-th measurement for the n-th BS with true value  $\alpha_{\triangleleft n, \bullet l}$ .

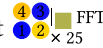
### 9.1 Outdoor Courtyard

Figure 12 illustrates the results of our outdoor measurements for the FFT according to Algorithm 1 and MuSiC according to Algorithm 2, respectively. The courtyard is of size 50 m × 30 m and contains shrubs, trees, benches, and a pond, being surrounded by walls (see Figure 10(a)). We set up



Fig. 10. Photos of the scenarios.

our system at a  $20\text{ m} \times 15\text{ m}$  subspace, which is the largest possible contiguous rectangle. Measurements are taken at 53 positions (measurement point 08–60), with the angular errors to the four BS visualized by colored circles and the final positioning errors visualized by colored rectangles.

For instance, the extract  from Figure 12 shows the number of the measurement point 25 for the FFT. The individual angular errors from BS 1 through 4 are represented by the colored circles and the error for the position estimate by the colored rectangle. The colors correspond to the associated color scales in the images. For this example, the angular errors for BS 1 through 4 are  $0.9^\circ$ ,  $40.2^\circ$ ,  $1.7^\circ$ , and  $45.3^\circ$ , respectively, and the position error is 3.5 m. Moreover, the location of the cross also indicates the true measurement position. The large green semicircles characterize bushes and trees in the courtyard. The four BS are located in the corners, and the Calibrator Station is placed in the center of the scenario. To determine the true measurement positions, we use a Leica Viva TS16 tachymeter exhibiting errors below 1 mm, referred to as the Total Station in the image.

Each BS is aligned such that the normal vector of the plane containing its 2.4-GHz antennas points in the direction toward the calibrator. Since it is difficult to find this orientation accurately, we initially perform a two-step process before making our actual measurements. First, we roughly align the normal vector of all BS in the direction of the calibrator. Second, we exploit the fact that all incident angles for the MS located at the position of the calibrator are ideally zero. Thus, in the following we fine-tune the orientations by rotating all BS slightly until some preliminary readings of the incident angles are close to zero. We then fix these alignments for our actual measurements.

We perform 10 repetitions at each spot. As a basis for evaluating our proposed methods, both pictures show only the results for the conventional maximum search together with clustering according to Section 5.2 as well as the simple iterative approach for positioning from Section 6.1. As can be seen clearly in the picture, MuSiC performs superior at any single spot. Considering all measurement points, there is a mean angle error of  $3.16^\circ$  and a mean positioning error of 0.80 m. For BS 2, there is an angular outlier at measurement point 49, which results in a positioning error of 8.48 m. Not including that location, the mean angle error and the mean positioning error decrease to  $2.95^\circ$  and 0.65 m, respectively. The maximum positioning error for all remaining spots is 1.59 m.<sup>14</sup> In contrast, the mean angular error for the FFT is already  $11.63^\circ$ , resulting in a mean

<sup>14</sup>Identifying outliers is difficult in practice. The results are listed only to demonstrate the potential of our system.

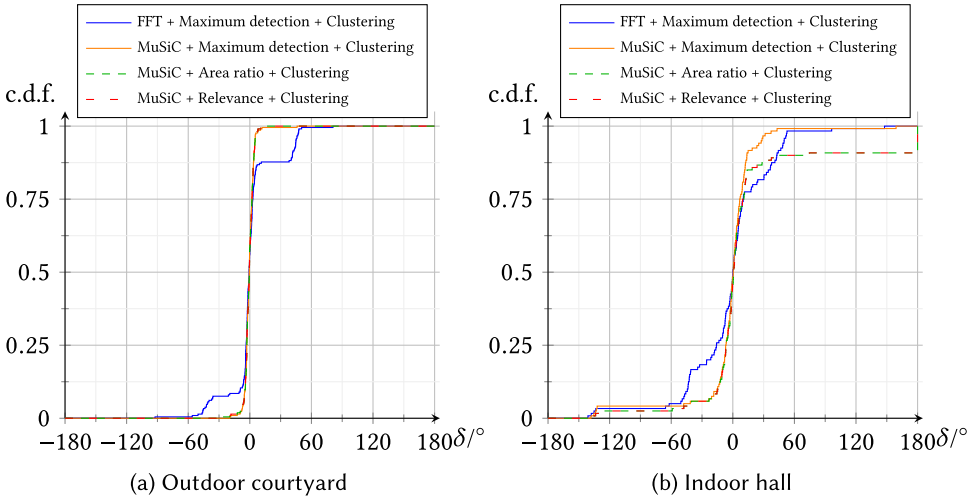


Fig. 11. Cumulative distribution functions for FFT and MuSiC for outdoors and indoors.

Table 2. Outdoor Measurement Results

Approach	Angle Error	Position Error
FFT, Maximum detection, Clustering, Iterative	11.63°	3.88 m
MuSiC, Maximum detection, Clustering, Iterative	3.16°	0.80 m
MuSiC, Area ratio, Weighted clustering, Iterative	3.07°	0.67 m
MuSiC, Relevance, Weighted clustering, Iterative	3.07°	0.67 m
MuSiC, Area ratio, Weighted clustering, Weighted iterative	3.07°	0.70 m
MuSiC, Relevance, Weighted clustering, Weighted iterative	3.07°	0.69 m

positioning error of 3.88 m.<sup>15</sup> These performance differences are also evident in Figure 11(a) for the **cumulative distribution functions (c.d.f.)**, which show a steep increase only for MuSiC. In contrast, the measurement errors for the FFT are clearly readable at the lower and upper plateau. It can also be seen that the differences between the different MuSiC variants (i.e., maximum detection, area ratio, and relevance) are small. Finally, Table 2 summarizes all results together with the outcomes of our proposed methods.

When using area ratio for clustering, the mean angle error decreases slightly. Please note that the angle error must always be the same for the associated iterative and weighted iterative variants, since it is calculated before the positioning step.<sup>16</sup> Subsequently, this leads to a 16% improvement in position accuracy. Similar results for the angle error are obtained for the relevance-based clustering with an improvement of 15% compared to the conventional maximum detection. The outlier of measurement point 49 disappears for both enhanced methods. Nonetheless, there are only minor differences in the results between the two methods, which may disappear with a larger sample.

The energy consumption in the different operating modes is briefly shown in the following. In idle mode, the system consumes about 0.87 W, whereas communication at 0.9 GHz and sending sinusoidal waves at 2.4 GHz requires 1.95 W. However, performing the FFT or MuSiC after receiving these sinusoidal waves slightly increases power consumption to 2.00 W.

<sup>15</sup>We refrained from outlier removal for the FFT, since there are many inferior measurements.

<sup>16</sup>Preliminary measurements have shown that  $t_{\text{prominence}} := 0.3$  is a good choice and is used in all experiments.

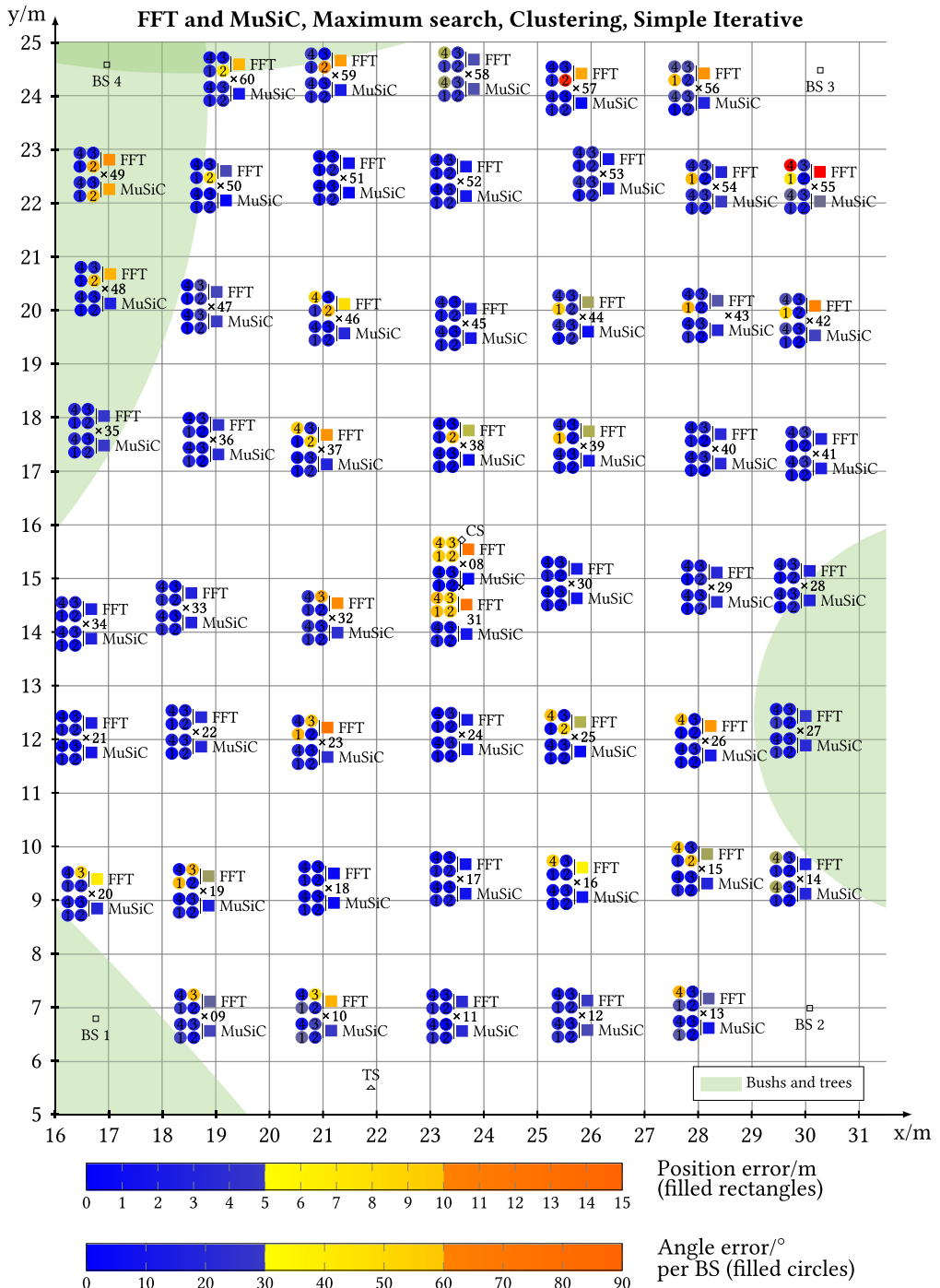


Fig. 12. Outdoor angle and positioning measurements for FFT and MuSiC (maximum search and clustering according to Section 5.2 and simple iterative from Section 6.1).

Table 3. Indoor Measurement Results

Approach	Angle Error	Position Error
FFT, Maximum detection, Clustering, Iterative	25.50°	3.39 m
MuSiC, Maximum detection, Clustering, Iterative	15.51°	2.09 m
MuSiC, Area ratio, Weighted clustering, Iterative	13.35°	2.17 <sup>a</sup>
MuSiC, Relevance, Weighted clustering, Iterative	13.34°	2.15 <sup>a</sup>
MuSiC, Area ratio, Weighted clustering, Weighted iterative	13.35°	1.68 m
MuSiC, Relevance, Weighted clustering, Weighted iterative	13.34°	1.66 m

<sup>a</sup>For area ratio and relevance, the special cases arise where angular information for some BS is missing for a few measurement points (e.g., BS 1 for measurement point 20). This is due to the shape of the respective spectra, where no local maxima with sufficient prominence can be found. Of course, the positioning is then performed with less data. In total, there are seven/two measurement points where information from one/two BS, respectively, is missing. This explains the slightly worse position error for area ratio and relevance compared to maximum detection, even if the angular errors are superior.

## 9.2 Indoor Hall

We perform our indoor measurements within a university hall of size 17 m × 13 m that contains stairs, handrails, pillars, and display cases (see Figure 10(b)). Due to these obstacles and the presence of walls, we expect a higher occurrence of multipath effects and thus lower positioning performance. The experiments are performed as before, including the BS alignment procedure.

As a basis for evaluating our proposed methods, Figure 13 shows the angular and positioning results for both FFT and MuSiC, using simple maximum search together with clustering as described in Section 5.2 and simple iterative search. Multipath effects are clearly visible (e.g., the reflection at the left wall leads to false readings for BS 1 at measuring points 35, 36 and 37). In contrast, similar false readings at the right side for BS 3 (e.g., for points 28, 29, and 30) are not recognizable due to the lecture hall adjoining by means of glass doors. Due to the adjacent corridors on the upper and lower transverse sides, there are also hardly any multipath effects there.

Table 3 illustrates the results for all variants. As expected, MuSiC is superior to FFT. However, compared to the outdoor experiments, the mean angular error and mean position error increase significantly. Although both area ratio and relevance variants appear to slightly degrade performance for the simple iterative positioning approach, they increase positioning accuracy by about 25% for the weighted alternative. Similar to the outdoor measurements, the results for relevance and area ratio are almost the same. Nevertheless, the data show a slight advantage for relevance, which may not be statistically significant. We intend to investigate this in a future publication.

The corresponding c.d.f. are depicted in Figure 11(b). Note that a drawback of the c.d.f. is that the influence of multipath effects on individual measuring points is hidden. The c.d.f. illustrate that the difference between the various MuSiC variants (i.e., maximum detection, area ratio, and relevance) is minor. This indicates that the strength of the novel methods lies, among other things, in the determination of the weights for subsequent positioning, which is not reflected in the c.d.f. either.

## 10 DISCUSSION

This work shows that in our experimental setups, MuSiC performs significantly better than the FFT for the ordinary maximum detection together with our initial clustering technique from Section 5.2 and the simple iterative approach from Section 6.1. Based on the considerations from Section 5.5, we refrained from applying the enhanced clustering algorithms from Sections 5.3 and 5.4 as well as the weighted positioning technique from Section 6.2 to the FFT.

As expected, the outdoor measurements are superior. Looking at the individual spectra for a fixed measurement point, it can be seen that the diversity of the spectra increases significantly for

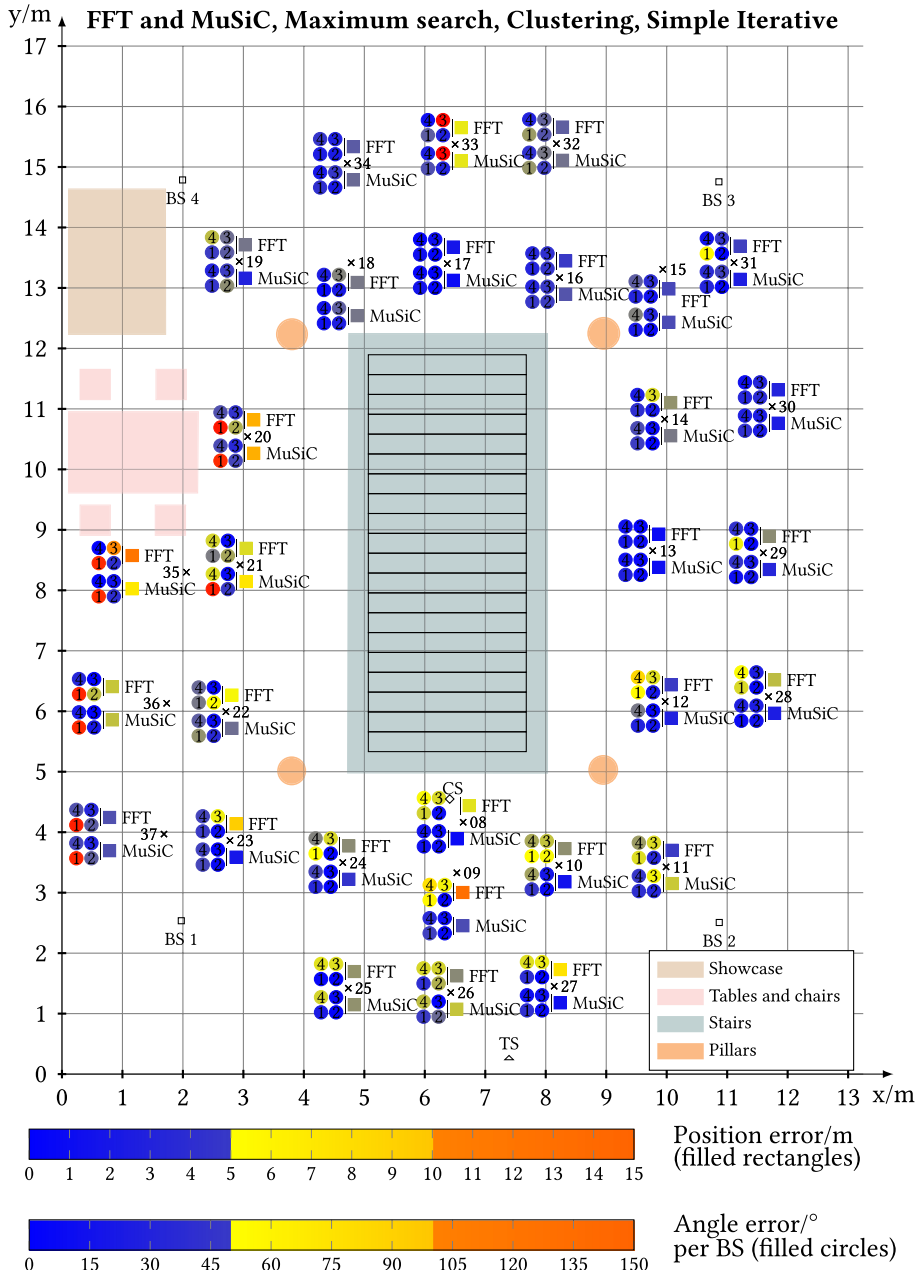


Fig. 13. Indoor angle and positioning measurements for FFT and MuSiC (maximum search and clustering according to Section 5.2 and simple iterative from Section 6.1).

indoors, similar to Figure 3 (being some extract for BS 3 for measurement point 10 of the outdoor measurement). This can be attributed to multipath effects. More precisely, propagation along NLoS (e.g., reflections from walls) is visible due to parasitic peaks in the spectra at the parasitic angles. That effect worsens near walls and is visible for our indoor measurement points 35, 36, or 37. In this regard, our novel methods show significant improvements on the position accuracy of 25%

indoors and 15% outdoors. It is noteworthy that both enhanced clustering techniques (i.e., the area ratio based and relevance based) perform almost equally well. This indicates the strong influence of weighted clustering on the overall results. However, this technique is only practical if the weights can be determined in the first place, which is made possible by our two new algorithms.

Our outdoor angle measurements for MuSiC applying either clustering technique are in line with the work of Morhart et al. [45], where outdoor targets are tracked at 2.4 GHz. With six antennas and a Kalman filter, they achieve a slightly better mean angular error of 2.0°. Comparable results for a ULA with eight quasi-Yagi antennas are reported in the work of Vu et al. [62]. In contrast to both, we present raw data where no motion of the MS occurs. Therefore, we expect improvements for our system when entity movement is allowed and the benefits of tracking filters come into play. Note that since the position of our entities is fixed during our measurements, systematic errors (e.g., due to multipath effects) cannot be easily detected. Incorrect NLoS angles for moving objects, however, are identified straightforward, since their values are constantly changing, whereas LoS angles remain almost constant.

The AoA-based part of the positioning system in the work of Chen et al. [11], which employs COTS SDR, works similarly to our system. Using only two antennas at each of the two BS, they report a mean position error of 2.0 m outdoors. Their system operates at 0.9 GHz and uses only the simple reference method.

ESPRIT is utilized in the work of Liu et al. [38], where a huge frequency band is generated by combining multiple non-overlapping channels. The system is specifically tailored for LoRa devices at 2.4 GHz and achieves a median indoor angle error of 1.2° and 6.0° at LoS and NLoS conditions, respectively. Compared to our system, they achieve slightly lower angular errors, which is due to the introduction of numerous virtual antennas. However, for the same number of BS, the position accuracy in our system is better, which can be attributed to our novel methods for determining the incident angle from the MuSiC spectra, as well as the cooperation with the weighted positioning algorithms.

Target tracking is investigated by Hu et al. [25]. They sequentially determine the time of flight difference between two antennas, where the accuracy is enhanced by rotating the structure. Compared to us, an improved median indoor error of 4.5° is reported. However, on the one hand, the mechanically rotating structure, which effectively introduces several new virtual antennas, makes it difficult to evaluate these results compared to this work. On the other hand, this system is only suitable for robots.

Kotaru et al. [31] employ the CSI from standard NIC, deriving the incident angles along with the ranges. Using four BS, they achieve a median localization error of 0.8 m. However, it is difficult to compare it to our work, since they improve their results by additionally determining ranges. Additionally, they perform measurements at 30 different frequencies, whereas we use only one. If we extend our system to execute measurements at many different frequencies, we can further enhance our system. In the work of Sen et al. [54], another approach to employing CSI is described, in which additional INS data is included. Utilizing five BS, they achieve a mean error of 2.0 m. Although they use more BS and an extra data source, our indoor position results are 17% better. A summary on related work is found in Table 4.

## 11 CONCLUSION AND FUTURE WORK

In this research work, a concept for AoA-based secondary RADAR positioning with cooperative targets using the transmission of sinusoidal waves of a specific frequency was developed. The corresponding theory as well as a feasibility study through hardware implementation and experimental characterization were carried out. After a detailed introduction of related work, the principle for coherent, non-coherent, quasi-coherent, and arbitrary signals was presented, with a

Table 4. Related Systems Employing MuSiC

Approach	Angle Error	Position Error	Remarks
[45]	2.0° (Outdoor)		<ul style="list-style-type: none"> <li>• Employs six antennas</li> <li>• Uses Kalman filter</li> <li>• Transmission frequency: 2.4 GHz</li> </ul>
[62]	2.0° (Lab)		<ul style="list-style-type: none"> <li>• Employs eight antennas</li> <li>• Transmission frequency: 2.4 GHz</li> </ul>
[11]		2.0 m (Outdoor)	<ul style="list-style-type: none"> <li>• Employs two antennas and two BS</li> <li>• Transmission frequency: 0.9 GHz</li> </ul>
[38]	1.2° <sup>a</sup> (Indoor)	2.4 m <sup>a</sup> (Indoor) 4.4 m <sup>a</sup> (Outdoor)	<ul style="list-style-type: none"> <li>• Employs two antennas and four BS</li> <li>• Transmission frequency: 2.4 GHz</li> </ul>
[25]	4.5° <sup>a</sup> (Indoor)		<ul style="list-style-type: none"> <li>• Employs two antennas</li> <li>• Transmission frequency: 2.4 GHz</li> </ul>
[31]		0.8 m (Indoor)	<ul style="list-style-type: none"> <li>• Employs three antennas and multiple BS</li> <li>• Based on CSI from standard NIC</li> <li>• Additionally determines ranges</li> <li>• Transmission frequency: 5.0 GHz</li> </ul>
[54]		2.0 m (Indoor)	<ul style="list-style-type: none"> <li>• Employs three antennas and multiple BS</li> <li>• Based on CSI from standard NIC</li> <li>• Additionally employs INS</li> <li>• Transmission frequency: 2.4/5.0 GHz</li> </ul>
This work	3.1° (Outdoor) 13.2° (Indoor)	0.7 m (Outdoor) 1.7 m (Indoor)	<ul style="list-style-type: none"> <li>• Employs four antennas and four BS</li> <li>• Hardware/firmware/software design</li> <li>• Transmission frequency: 2.4 GHz</li> </ul>

<sup>a</sup>This is the median.

special emphasis on the study of two algorithms, namely FFT and MuSiC. Especially for the latter, comprehensive derivations of the corresponding theory can be found in the appendix. In addition, the appendix contains some theoretical proofs on the complex signal covariance matrices, which, to the best of the authors' knowledge, cannot be found in the literature (most sources assume non-complex behavior, which is not correct since I/Q-data are complex). Moreover, the traditional method of deriving the incidence angles from the spectrum was introduced along with our improved clustering techniques. Together with the probable incidence angles, they provide a measure of the trust of the result. These were included in the derivation of the position using weights. In this regard, the article includes a text on two contrasting positioning techniques. Further on, simulations were performed on important signal parameters. These were considered for the hardware, firmware, and software developed to prove the concept. We conducted tests in a simple outdoor environment where we achieved a mean position error of 0.80 m for basic maximum detection and clustering along with simple iterative. Using our novel techniques reduced the error by 15%. However, tests in a challenging indoor multipath environment showed improvements of 25%. All results were obtained by using only four BS. In the last section, we compared our results with related works, reflecting the good performance of our system. In this research, we did not implement tracking filters to directly visualize the raw positioning performance. We defer this to future work.

## APPENDICES

### A HARDWARE DESIGN

In the following, three important hardware design parameters are examined in more detail.

#### A.1 Antenna Distance

Since we plan to use MuSiC among others, we investigate the influence of the antenna spacing  $a$  on the accuracy. In the work of Huang et al. [26], it is shown that the error decreases with increasing  $a$ . Moreover, it is added in the work of Mohanna et al. [43] that the optimal distance is close to  $0.5\lambda$  and that ambiguities occur for  $a > 0.6\lambda$ . For our design, we define  $a := 0.5\lambda$  using the highest possible frequency as recommended in the work of Tang [59], namely 2483.5 MHz for the Atmel AT86RF215. In doing so, we have  $a = 0.5\lambda = 0.5 c/f = 6.04$  cm.

#### A.2 Antenna Characteristics

Since the antennas of all BS should be at the same height above the ground, we apply antennas of type W1043 from Pulse Electronics with a very symmetrical horizontal radiation pattern to exclude influences of the antenna characteristics on the MuSiC spectra.

#### A.3 Clock Generation

All transceiver ICs are supplied with a clock of 26 MHz. As already mentioned, the phase relations between the ICs are crucial. All are connected to the same clock to avoid frequency drifts. Therefore, we use a voltage-controlled, temperature-compensated crystal oscillator that is placed in the center of the transceiver. During the design, we made sure that the wires between the crystal and all transceivers are almost the same length. A second criterion was to minimize the overall clock lengths to reduce capacitive loads.

## B COMPLEX RANDOM VARIABLES AND VECTORS

According to Park [47], a complex random variable  $\tilde{z} = \tilde{x} + i\tilde{y}$  can be considered a real bivariate random vector  $(\tilde{x}, \tilde{y})^T$ . Equally, a complex random vector  $\tilde{z} = \tilde{\mathbf{x}} + i\tilde{\mathbf{y}}$  of size N can be interpreted as real vector  $(\tilde{\mathbf{x}}, \tilde{\mathbf{y}})^T$  of size  $2N$  with its components as the real and imaginary parts of the complex vector.

## C MUSIC: COMPLETE DERIVATION

In the following, we provide the complete derivation for MuSiC. All requirements from Section 4.2 apply. We additionally require narrow-band sending signals (i.e., the bandwidth is well below the sending frequency). Assuming this, the propagation delay between the receiving antennas is constant, and thus according to Roy and Kailath [52] the envelope can be considered constant for the short period to travel from one receiving antenna to the next, simplifying derivations. Certainly in the case of pure sinusoidal transmission, the narrow-band assumption holds and the envelope being the amplitude of the sine is constant by definition. In any case, since  $\hat{s}_{rf,[S_m]} := \hat{s}_{rf,[S_m]}(t)$  can be considered constant, phasor transform to Equations (20) and (21) is applied to have<sup>17</sup>

$$s_{rf,[S_m] \rightarrow R}(t) = \hat{s}_{rf,[S_m]} \exp(j\omega_{rf,[S_m]} t) \exp(j\varphi_{rf,[S_m]}) \quad (43)$$

<sup>17</sup>By converting from the time domain to the frequency domain, we obtain simpler formulas.

and

$$\begin{aligned} \underline{s}_{\text{rf},S_m \rightarrow R_n}(t) &= \hat{s}_{\text{rf},[S_m]} \exp \left( j \omega_{\text{rf},[S_m]} \left[ t - \frac{d_1}{c} - \frac{\Delta d_n}{c} \right] \right) \exp \left( j \varphi_{\text{rf},[S_m]} \right) \\ &= \underbrace{\frac{\hat{s}_{\text{rf},[S_m]} \exp(j\varphi_{\text{rf},[S_m]})}{\exp(j\omega_{\text{rf},[S_m]} \frac{d_1}{c})}}_{:=K_{\text{rf},S_m}} \exp(j\omega_{\text{rf},[S_m]} t) \underbrace{\exp \left( -j \omega_{\text{rf},[S_m]} \frac{\Delta d_n}{c} \right)}_{:=a_{S_m:R_1 \rightarrow [R_n]}(\alpha_{\triangleleft \bullet})}. \end{aligned} \quad (44)$$

Integrating all  $a_{S_m:R_1 \rightarrow [R_n]}(\alpha_{\triangleleft \bullet})$  within one matrix, denoted as steering matrix  $\underline{A}$ , we have

$$\underline{A} := \begin{pmatrix} a_{S_1:R_1 \rightarrow [R_1]}(\alpha_{\triangleleft \bullet}) & a_{S_2:R_1 \rightarrow [R_1]}(\alpha_{\triangleleft \bullet}) & \dots & a_{S_M:R_1 \rightarrow [R_1]}(\alpha_{\triangleleft \bullet}) \\ a_{S_1:R_1 \rightarrow [R_2]}(\alpha_{\triangleleft \bullet}) & a_{S_2:R_1 \rightarrow [R_2]}(\alpha_{\triangleleft \bullet}) & \dots & a_{S_M:R_1 \rightarrow [R_2]}(\alpha_{\triangleleft \bullet}) \\ \vdots & \vdots & \ddots & \vdots \\ a_{S_1:R_1 \rightarrow [R_N]}(\alpha_{\triangleleft \bullet}) & a_{S_2:R_1 \rightarrow [R_N]}(\alpha_{\triangleleft \bullet}) & \dots & a_{S_M:R_1 \rightarrow [R_N]}(\alpha_{\triangleleft \bullet}) \end{pmatrix}. \quad (45)$$

The signal received  $\underline{s}_{\text{rf},R_n}$  at antenna  $R_n$  is a superimposition of all received source signals. We include AWGN—that is,

$$\underline{s}_{\text{rf},[R_n]}(t) = \tilde{n}_{\text{rf},[R_n]}(t) + \sum_{m=1}^M \underline{s}_{\text{rf},S_m \rightarrow [R_n]}(t) = \tilde{n}_{\text{rf},[R_n]}(t) + \sum_{m=1}^M \underline{s}_{\text{rf},S_m \rightarrow [R_1]}(t) \cdot a_{S_m:R_1 \rightarrow [R_n]}(\alpha_{\triangleleft \bullet}). \quad (46)$$

Random variables are identified by a tilde superscript. The last equality results from referring to the received signal at the first antenna using Equation (44). Employing matrix notation, it holds

$$\begin{pmatrix} \tilde{s}_{\text{rf},[R_1]}(t) \\ \vdots \\ \tilde{s}_{\text{rf},[R_N]}(t) \end{pmatrix} = \begin{pmatrix} \tilde{n}_{\text{rf},[R_1]}(t) \\ \vdots \\ \tilde{n}_{\text{rf},[R_N]}(t) \end{pmatrix} + \underline{A} \begin{pmatrix} \underline{s}_{\text{rf},S_1 \rightarrow [R_1]}(t) \\ \vdots \\ \underline{s}_{\text{rf},S_M \rightarrow [R_1]}(t) \end{pmatrix}. \quad (47)$$

Thus,  $\underline{s}_{\text{rf},[\mathbb{R}]}(t)$  is the vector of the continuous phasor signals at all antennas. In the following, we assume that  $\underline{s}_{\text{rf},[\mathbb{R}]}(t)$  and  $\tilde{n}_{\text{rf},[\mathbb{R}]}(t)$  are complex stationary ergodic processes, which implies that its timely average is identical to its expected value at a fixed point in time [42]. Since the average of a sinusoidal wave is zero and noise is assumed to be zero mean, the expected value of  $\tilde{s}_{\text{rf},[\mathbb{R}]}(t)$  at a fixed instance of time  $t$  is zero. To obtain tidy formulas, we do not carry the time dependence at fixed  $t$  for any variable below—that is, instead of  $\tilde{s}_{\text{rf},[\mathbb{R}]}(t)$ ,  $\tilde{n}_{\text{rf},[\mathbb{R}]}(t)$ , and  $\underline{s}_{\text{rf},S \rightarrow [R_1]}(t)$ , we briefly write  $\tilde{s}_{\text{rf},[\mathbb{R}]}$ ,  $\tilde{n}_{\text{rf},[\mathbb{R}]}$ , and  $\underline{s}_{\text{rf},S \rightarrow [R_1]}$ . Next, the covariance matrix of size  $N \times N$  is set up:

$$\text{COV}\{\tilde{s}_{\text{rf},[\mathbb{R}]}\} := \mathbb{E}\{\tilde{s}_{\text{rf},[\mathbb{R}]} \tilde{s}_{\text{rf},[\mathbb{R}]}^H\} - \underbrace{\mathbb{E}\{\tilde{s}_{\text{rf},[\mathbb{R}]}\}}_{=0} \underbrace{\mathbb{E}\{\tilde{s}_{\text{rf},[\mathbb{R}]}^H\}}_{=0}. \quad (48)$$

Here,  $X^H$  is the adjoint matrix of matrix  $X$ . Certainly,  $\text{COV}\{\tilde{s}_{\text{rf},[\mathbb{R}]}\}$  is Hermitian.<sup>18</sup> Employing Equation (47), it is valid

<sup>18</sup>The diagonal elements are real, since for any complex number  $z$ :  $z \cdot z^* \in \mathbb{R}$ , where  $z^*$  is the conjugate complex of  $z$ . Moreover, the non-diagonal elements and the elements mirrored on the main diagonal are conjugate complex, since for any two complex numbers  $z_1$  and  $z_2$  it is true that  $(z_1 \cdot z_2)^* = z_1^* \cdot z_2$ .

$$\begin{aligned}
& \text{COV} \left\{ \tilde{s}_{\text{rf},[\mathbb{R}]} \right\} \\
&= \mathbb{E} \left\{ \left( \tilde{n}_{\text{rf},[\mathbb{R}]} + \underline{A} s_{\text{rf},S \rightarrow [\mathbb{R}_1]} \right) \left( \tilde{n}_{\text{rf},[\mathbb{R}]} + \underline{A} s_{\text{rf},S \rightarrow [\mathbb{R}_1]} \right)^H \right\} = \mathbb{E} \left\{ \left( \tilde{n}_{\text{rf},[\mathbb{R}]} + \underline{A} s_{\text{rf},S \rightarrow [\mathbb{R}_1]} \right) \left( \tilde{n}_{\text{rf},[\mathbb{R}]}^H + s_{\text{rf},S \rightarrow [\mathbb{R}_1]}^H \underline{A}^H \right) \right\} \\
&= \mathbb{E} \left\{ \tilde{n}_{\text{rf},[\mathbb{R}]} \tilde{n}_{\text{rf},[\mathbb{R}]}^H \right\} + \mathbb{E} \left\{ \tilde{n}_{\text{rf},[\mathbb{R}]} s_{\text{rf},S \rightarrow [\mathbb{R}_1]}^H \right\} \underline{A}^H + \underline{A} \mathbb{E} \left\{ s_{\text{rf},S \rightarrow [\mathbb{R}_1]} \tilde{n}_{\text{rf},[\mathbb{R}]}^H \right\} + \underline{A} \mathbb{E} \left\{ s_{\text{rf},S \rightarrow [\mathbb{R}_1]} s_{\text{rf},S \rightarrow [\mathbb{R}_1]}^H \right\} \underline{A}^H \\
&= \mathbb{E} \left\{ \tilde{n}_{\text{rf},[\mathbb{R}]} \tilde{n}_{\text{rf},[\mathbb{R}]}^H \right\} + \underbrace{\mathbb{E} \left\{ \tilde{n}_{\text{rf},[\mathbb{R}]} \right\} \mathbb{E} \left\{ s_{\text{rf},S \rightarrow [\mathbb{R}_1]}^H \right\}}_{=0} \underline{A}^H + \underline{A} \mathbb{E} \left\{ s_{\text{rf},S \rightarrow [\mathbb{R}_1]} \right\} \underbrace{\mathbb{E} \left\{ \tilde{n}_{\text{rf},[\mathbb{R}]}^H \right\}}_{=0} + \underline{A} \mathbb{E} \left\{ s_{\text{rf},S \rightarrow [\mathbb{R}_1]} s_{\text{rf},S \rightarrow [\mathbb{R}_1]}^H \right\} \underline{A}^H \\
&= \mathbb{E} \left\{ \tilde{n}_{\text{rf},[\mathbb{R}]} \tilde{n}_{\text{rf},[\mathbb{R}]}^H \right\} + \underline{A} \underbrace{\mathbb{E} \left\{ s_{\text{rf},S \rightarrow [\mathbb{R}_1]} s_{\text{rf},S \rightarrow [\mathbb{R}_1]}^H \right\}}_{=\text{COV} \left\{ s_{\text{rf},S \rightarrow [\mathbb{R}_1]} \right\}} \underline{A}^H. \\
&= \text{COV} \left\{ \tilde{n}_{\text{rf},[\mathbb{R}]} \right\} + \text{COV} \left\{ s_{\text{rf},S \rightarrow [\mathbb{R}_1]} \right\} \underline{A}^H. \tag{49}
\end{aligned}$$

since the expectation is a linear operator, where a constant matrix can be factored out. Moreover, in the fourth equality, we used that noise and signal are uncorrelated. Please note that the expectation operator in the second term in the fifth equality could be neglected, since  $s_{\text{rf},S \rightarrow [\mathbb{R}_1]} s_{\text{rf},S \rightarrow [\mathbb{R}_1]}^H$  is a constant (please note that  $s_{\text{rf},S \rightarrow [\mathbb{R}_1]}$  is the true value and not a random variable).

Since the marginal distributions for the noise are uncorrelated, the noise covariance matrix must be a diagonal matrix. It is derived in detail in Appendix D and reads

$$\text{COV} \left\{ \tilde{n}_{\text{rf},[\mathbb{R}]} \right\} = \sigma^2 \mathbf{I}. \tag{50}$$

Practically, neither  $\text{COV} \left\{ \tilde{s}_{\text{rf},[\mathbb{R}]} \right\}$  nor  $\text{COV} \left\{ s_{\text{rf},S \rightarrow [\mathbb{R}_1]} \right\}$  are known, but since  $\tilde{s}_{\text{rf},[\mathbb{R}]}(t)$  can be measured at multiple points of time at the antenna elements, we can come up with an estimator for its covariance, denoted as  $\widetilde{\text{COV}} \left\{ \tilde{s}_{\text{rf},[\mathbb{R}]} \right\}$ . Let us assume that sampling at D different sampling points  $t_1, \dots, t_D$  of this vector is performed and a sampling matrix for these signals is set up—that is,

$$\widetilde{\text{COV}} \left\{ \tilde{s}_{\text{rf},[\mathbb{R}]} \right\} := \frac{1}{N} \tilde{S}_{\text{rf},[\mathbb{R}]} (t_1, \dots, t_D) \tilde{S}_{\text{rf},[\mathbb{R}]}^H (t_1, \dots, t_D) \tag{51}$$

where

$$\tilde{S}_{\text{rf},[\mathbb{R}]} (t_1, \dots, t_D) := \left( \tilde{s}_{\text{rf},[\mathbb{R}]} (t_1) \tilde{s}_{\text{rf},[\mathbb{R}]} (t_2) \dots \tilde{s}_{\text{rf},[\mathbb{R}]} (t_D) \right) = \begin{pmatrix} \tilde{s}_{\text{rf},[\mathbb{R}_1]} (t_1) & \tilde{s}_{\text{rf},[\mathbb{R}_1]} (t_2) & \dots & \tilde{s}_{\text{rf},[\mathbb{R}_1]} (t_D) \\ \vdots & \vdots & \ddots & \vdots \\ \tilde{s}_{\text{rf},[\mathbb{R}_N]} (t_1) & \tilde{s}_{\text{rf},[\mathbb{R}_N]} (t_2) & \dots & \tilde{s}_{\text{rf},[\mathbb{R}_N]} (t_D) \end{pmatrix}. \tag{52}$$

is characterized as signal matrix.

The noise covariance matrix  $\text{COV} \left\{ \tilde{n}_{\text{rf},[\mathbb{R}]} \right\}$  is a multiple of the identity matrix with rank N, as shown in Appendix D. Moreover, it is proven in Appendix E that the covariance matrix without noise  $\text{COV} \left\{ \tilde{s}_{\text{rf},[\mathbb{R}]} \right\}$  or its sampled version  $\widetilde{\text{COV}} \left\{ \tilde{s}_{\text{rf},[\mathbb{R}]} \right\}$  is Hermitian and of rank M. Finally, in Appendix F, we derive the eigenvalues of the Hermitian covariance matrix with noise. These are a set of the M eigenvalues  $\lambda_1, \dots, \lambda_M$  which can be associated to the incident signals and the remaining  $N - M$  eigenvalues  $\lambda_{M+1}, \dots, \lambda_N$  belonging to noise. Moreover, let  $\mathbf{v}_1, \dots, \mathbf{v}_M$  and  $\mathbf{v}_{M+1}, \dots, \mathbf{v}_{N-M}$  be the related eigenvectors (being real since they are the eigenvectors of a Hermitian matrix). Thus, it is especially true for the noise eigenvalues and eigenvectors that ( $i \in [M + 1, N]$ )

$$\text{COV} \left\{ \tilde{s}_{\text{rf},[\mathbb{R}]} \right\} \mathbf{v}_i = \lambda_i \mathbf{v}_i \quad ; \quad \mathbf{v}_i \neq 0 \tag{53}$$

where  $\lambda_i = \sigma^2$  according to Appendix F. Inserting Equations (49) and (50), we first have

$$\left( \sigma^2 \mathbf{I} + \underline{\mathbf{A}} \mathbf{C} \mathbf{O} \mathbf{V} \left\{ \underline{s}_{\text{rf},S \rightarrow [\mathbb{R}_1]} \right\} \underline{\mathbf{A}}^H \right) \mathbf{v}_i = \sigma^2 \mathbf{v}_i. \quad (54)$$

After rearranging

$$\left( \sigma^2 \mathbf{v}_i + \underline{\mathbf{A}} \mathbf{C} \mathbf{O} \mathbf{V} \left\{ \underline{s}_{\text{rf},S \rightarrow [\mathbb{R}_1]} \right\} \underline{\mathbf{A}}^H \right) \mathbf{v}_i = \sigma^2 \mathbf{v}_i \quad (55)$$

and finally we obtain

$$\underline{\mathbf{A}} \mathbf{C} \mathbf{O} \mathbf{V} \left\{ \underline{s}_{\text{rf},S \rightarrow [\mathbb{R}_1]} \right\} \underline{\mathbf{A}}^H \mathbf{v}_i = 0. \quad (56)$$

Multiplying by  $(\mathbf{C} \mathbf{O} \mathbf{V} \left\{ \underline{s}_{\text{rf},S \rightarrow [\mathbb{R}_1]} \right\})^{-1} (\underline{\mathbf{A}}^H \underline{\mathbf{A}})^{-1} \underline{\mathbf{A}}^H$ , it holds

$$\underline{\mathbf{A}}^H \mathbf{v}_i = 0 \quad ; \quad \mathbf{v}_i \neq 0. \quad (57)$$

Please note that according to Equation (70) in Appendix E,  $\mathbf{C} \mathbf{O} \mathbf{V} \left\{ \underline{s}_{\text{rf},S \rightarrow [\mathbb{R}_1]} \right\}$  is regular, enabling to perform the inverse. Similarly, this is true for  $\underline{\mathbf{A}}^H \underline{\mathbf{A}}$  (see Equation (72)). The corresponding N – M noise eigenvectors  $\mathbf{v}_{M+1}, \dots, \mathbf{v}_{N-M}$  are concentrated within a matrix  $V_{\text{Noise}}$  of size  $N \times M$  characterizing the noise sub-space—that is,

$$V_{\text{Noise}} := \begin{pmatrix} \mathbf{v}_{M+1} & \mathbf{v}_{M+2} & \dots & \mathbf{v}_N \end{pmatrix}. \quad (58)$$

As a last step, an angle-dependent pseudo-spectrum is generated. Therefore, a steering vector  $\underline{\mathbf{a}}(\alpha_{\ll \bullet})$  is set up, based on the specification of  $\underline{a}_{S_m; R_1 \rightarrow [\mathbb{R}_n]}(\alpha_{\ll \bullet})$  in Equation (44)—that is,

$$\underline{\mathbf{a}}(\alpha_{\ll \bullet}) := \begin{pmatrix} 1 & \exp \left( -j \omega_{\text{rf},[\mathbb{S}_m]} \frac{\Delta d_2}{c} \right) & \dots & \exp \left( -j \omega_{\text{rf},[\mathbb{S}_m]} \frac{\Delta d_N}{c} \right) \end{pmatrix}^T. \quad (59)$$

As before,  $\alpha_{\ll \bullet}$  is the angle. For any desired selection of angles, the pseudo-spectrum may be calculated, which shall contain a peak at every angle being equal to an incident angle. Certainly, Equation (57) must be considered by such a spectrum. Thus, a very simple pseudo-spectrum P is

$$P(\alpha_{\ll \bullet}) = \frac{1}{\left( \underline{\mathbf{a}}(\alpha_{\ll \bullet})^H V_{\text{Noise}} \right)^H \left( \underline{\mathbf{a}}(\alpha_{\ll \bullet})^H V_{\text{Noise}} \right)} = \frac{1}{\left( V_{\text{Noise}}^H \underline{\mathbf{a}}(\alpha_{\ll \bullet}) \underline{\mathbf{a}}(\alpha_{\ll \bullet})^H V_{\text{Noise}} \right)}. \quad (60)$$

Actually, according to Equation (57), all coordinates must be checked individually. Building up the pseudo-spectrum as earlier allows us to test all components in parallel and to reduce the result to a real value, where we get maxima due to the division.

## D STRUCTURE OF NOISE COVARIANCE MATRIX FOR MUSIC

The noise vector  $\tilde{\mathbf{n}}_{\text{rf},[\mathbb{R}]}$  is a column vector of N complex random variables and thus can be considered a real random vector of size  $2N$  for its real and imaginary components. In the following, we assume that this real noise vector can be modeled as multi-variate Gaussian distribution of dimension  $2N$ , where its marginal distributions are stochastically independent Gaussian random variables with zero mean and variance  $1/2\sigma^2$ . In doing so, the distribution for this noise vector  $\tilde{\mathbf{n}}_{\text{rf},[\mathbb{R}]} = (\Re(\tilde{\mathbf{n}}_{\text{rf},[\mathbb{R}]}), \Im(\tilde{\mathbf{n}}_{\text{rf},[\mathbb{R}]}))^T$ , where  $\Re(\tilde{\mathbf{n}}_{\text{rf},[\mathbb{R}]})$  is the vector of the real parts of  $\tilde{\mathbf{n}}_{\text{rf},[\mathbb{R}]}$  and similarly  $\Im(\tilde{\mathbf{n}}_{\text{rf},[\mathbb{R}]})$  as the vector of the imaginary parts, reads

$$f_{\tilde{\mathbf{n}}_{\text{rf},[\mathbb{R}]}}(\mathbf{n}_{\text{rf},[\mathbb{R}]}) = \frac{1}{\sqrt{(2\pi)^{2N} \det[\Sigma]}} \exp \left( -\frac{1}{2} \mathbf{n}_{\text{rf},[\mathbb{R}]}^T \Sigma^{-1} \mathbf{n}_{\text{rf},[\mathbb{R}]} \right). \quad (61)$$

Certainly, the covariance matrix  $\Sigma$  of size  $[2N, 2N]$  for  $\tilde{\mathbf{n}}_{\text{rf},[\mathbb{R}]}$  is ( $I$  is the identity matrix)

$$\text{COV} \left\{ \tilde{\mathbf{n}}_{\text{rf},[\mathbb{R}]} \right\} = \Sigma = \begin{pmatrix} 1/2\sigma^2 & 0 & \dots & 0 \\ 0 & 1/2\sigma^2 & \dots & 0 \\ \vdots & \vdots & \ddots & \vdots \\ 0 & 0 & \dots & 1/2\sigma^2 \end{pmatrix} = \text{diag} \left( \frac{1}{2}\sigma^2, \frac{1}{2}\sigma^2, \dots, \frac{1}{2}\sigma^2 \right) = \frac{1}{2}\sigma^2 I \quad (62)$$

because its marginal distributions are uncorrelated (especially for the two-dimensional case, see the work of Lindgren [36] and Mood [44]). Since it is true that for any complex random vector  $\tilde{\mathbf{z}} = \tilde{\mathbf{x}} + i\tilde{\mathbf{y}}$  [47]

$$\text{COV} \left\{ \tilde{\mathbf{z}} \right\} = \text{COV} \left\{ \tilde{\mathbf{x}} \right\} + \text{COV} \left\{ \tilde{\mathbf{y}} \right\} + i(\text{COV} \left\{ \tilde{\mathbf{y}}, \tilde{\mathbf{x}} \right\} - \text{COV} \left\{ \tilde{\mathbf{x}}, \tilde{\mathbf{y}} \right\}) \quad (63)$$

and since  $\tilde{\mathbf{x}}$  and  $\tilde{\mathbf{y}}$  are independent (i.e.,  $\text{COV} \left\{ \tilde{\mathbf{x}}, \tilde{\mathbf{y}} \right\} = \text{COV} \left\{ \tilde{\mathbf{y}}, \tilde{\mathbf{x}} \right\} = 0$ ), we obtain the covariance matrix of size  $[N, N]$  for the complex random vector as

$$\text{COV} \left\{ \tilde{\mathbf{n}}_{\text{rf},[\mathbb{R}]} \right\} = \text{diag} \left( 2 \cdot \frac{1}{2}\sigma^2, 2 \cdot \frac{1}{2}\sigma^2, \dots, 2 \cdot \frac{1}{2}\sigma^2 \right) = \sigma^2 I. \quad (64)$$

Due to its special structure, the noise covariance matrix has  $N$  identical eigenvalues  $\sigma^2$  with  $N$  orthogonal eigenvectors.

## E STRUCTURE OF SAMPLE COVARIANCE MATRIX FOR MUSIC WITHOUT NOISE

In the following, we analyze the sample covariance matrix in Equation (51) in the absence of noise. As an interim step, we need to examine the signal matrix from Equation (52). In that case, according to Equation (47), we have

$$\tilde{\mathbf{s}}_{\text{rf},[\mathbb{R}]}(t) = \underline{\mathbf{A}} \underline{\mathbf{s}}_{\text{rf},S \rightarrow [\mathbb{R}_1]}(t) \quad (65)$$

where  $\underline{\mathbf{s}}_{\text{rf},S \rightarrow [\mathbb{R}_1]}(t)$  is the true vector of the emitted signals of the  $M$  independent sending sources, received at the first antenna. To investigate that signal matrix, we need to go one step further to compile the first antenna sampling matrix (containing only true values)—that is,

$$\underline{\mathbf{S}}_{\text{rf},S \rightarrow [\mathbb{R}_1]}(t_1, \dots, t_D) := \begin{pmatrix} \underline{s}_{\text{rf},S_1 \rightarrow [\mathbb{R}_1]}(t_1) & \underline{s}_{\text{rf},S_1 \rightarrow [\mathbb{R}_1]}(t_2) & \dots & \underline{s}_{\text{rf},S_1 \rightarrow [\mathbb{R}_1]}(t_D) \\ \vdots & \vdots & \ddots & \vdots \\ \underline{s}_{\text{rf},S_M \rightarrow [\mathbb{R}_1]}(t_1) & \underline{s}_{\text{rf},S_M \rightarrow [\mathbb{R}_1]}(t_2) & \dots & \underline{s}_{\text{rf},S_M \rightarrow [\mathbb{R}_1]}(t_D) \end{pmatrix}. \quad (66)$$

If these sending sources emit independent signals, such as sinusoidal waves with different frequencies that are not multiple of each other, then, according to the FT, each transmitting signal cannot be recombined using the other sending signals [40]. If one chooses  $D$  sufficiently large, the same is true for  $\underline{\mathbf{S}}_{\text{rf},S \rightarrow [\mathbb{R}_1]}(t_1, \dots, t_D)$ . Mathematically speaking, that matrix is regular—that is,

$$\text{rank} \left( \underline{\mathbf{S}}_{\text{rf},S \rightarrow [\mathbb{R}_1]}(t_1, \dots, t_D) \right) = M. \quad (67)$$

It can easily be shown that  $\underline{\mathbf{A}}$ , being a  $N \times M$  matrix has rank  $M$ , since we assumed before  $N > M$ . Moreover, it is generally true for matrices over an arbitrary field  $\underline{\mathbf{X}}$  of size  $R \times S$  and  $\underline{\mathbf{Y}}$  of size  $S \times T$  that  $\text{rank}(\underline{\mathbf{X}}) + \text{rank}(\underline{\mathbf{Y}}) - S \leq \text{rank}(\underline{\mathbf{X}} \underline{\mathbf{Y}}) \leq \min(\text{rank}(\underline{\mathbf{X}}), \text{rank}(\underline{\mathbf{Y}}))$  [1]. Thus, we have

$$\begin{aligned} & \text{rank}(\underline{\mathbf{A}}) + \text{rank} \left( \underline{\mathbf{S}}_{\text{rf},S \rightarrow [\mathbb{R}_1]}(t_1, \dots, t_D) \right) - M \\ & \leq \text{rank} \left( \underline{\mathbf{A}} \underline{\mathbf{S}}_{\text{rf},S \rightarrow [\mathbb{R}_1]}(t_1, \dots, t_D) \right) \\ & \leq \min \left( \text{rank}(\underline{\mathbf{A}}), \text{rank} \left( \underline{\mathbf{S}}_{\text{rf},S \rightarrow [\mathbb{R}_1]}(t_1, \dots, t_D) \right) \right) \end{aligned} \quad (68)$$

and finally for the signal matrix

$$\begin{aligned} \text{rank}\left(\underbrace{\underline{\mathbf{A}} \underline{\mathbf{S}}_{\text{rf}, \text{S} \rightarrow \text{R}_1}(t_1, \dots, t_D)}_{=\tilde{\underline{\mathbf{S}}}_{\text{rf}, \text{R}}(t_1, \dots, t_D)}\right) &= M. \end{aligned} \quad (69)$$

If the preceding formula is used again, the following also applies

$$\text{rank}\left(\tilde{\underline{\mathbf{S}}}_{\text{rf}, \text{R}}(t_1, \dots, t_D)\tilde{\underline{\mathbf{S}}}_{\text{rf}, \text{R}}(t_1, \dots, t_D)^H\right) = M, \quad (70)$$

and considering Equation (51), we finally obtain

$$\text{rank}\left(\mathbf{E} \widetilde{\text{COV}}\left\{\tilde{\underline{\mathbf{s}}}_{\text{rf}, \text{R}}\right\}\right) = M. \quad (71)$$

Since  $\text{COV}\{\tilde{\underline{\mathbf{s}}}_{\text{rf}, \text{R}}\}$  and hence  $\mathbf{E} \widetilde{\text{COV}}\{\tilde{\underline{\mathbf{s}}}_{\text{rf}, \text{R}}\}$  are Hermitian, their rank is identical to the number of non-zero eigenvalues.<sup>19</sup>

It is only mentioned in passing that  $\text{rank}(\underline{\mathbf{A}}^H \underline{\mathbf{A}}) = M$ , since

$$\text{rank}\left(\underline{\mathbf{A}}^H\right) + \text{rank}\left(\underline{\mathbf{A}}\right) - M \leq \text{rank}\left(\underline{\mathbf{A}}^H \underline{\mathbf{A}}\right) \leq \min\left(\text{rank}\left(\underline{\mathbf{A}}^H\right), \text{rank}\left(\underline{\mathbf{A}}\right)\right). \quad (72)$$

## F STRUCTURE OF SAMPLE COVARIANCE MATRIX FOR MUSIC WITH NOISE

We are interested in the rank of the covariance matrix from Equation (49) in the presence of noise. In Appendix D, it was shown that the noise covariance matrix is a multiple of an identity matrix and of rank N. Additionally, Appendix E reveals that the covariance matrix without noise is Hermitian and of rank M. We are interested in the sum of both according to Equation (49). It can easily be shown that the eigenvalues of the sum of an Hermitian matrix  $\underline{\mathbf{X}}$  (size R × R) and a multiple of an identity matrix  $c\underline{\mathbf{I}}$  are  $\lambda_1 + c, \dots, \lambda_R + c$ , where  $\lambda_1, \dots, \lambda_R$  are the eigenvalues of  $\underline{\mathbf{X}}$ , possibly being zero (if  $\text{rank}(\underline{\mathbf{X}}) < R$ ). Thus, the eigenvalues of the covariance matrix are a set of the M eigenvalues that can be assigned to the incident signals, and the remaining  $N - M$  eigenvalues belong to noise.

## G VARIANCE FOR SIMPLE WEIGHTED ITERATIVE

We seek terms for the variances in Equation (36), where all random variables  $\tilde{\varepsilon}_n$  are assumed independent:

$$\begin{aligned} \text{Var}\{\tilde{\varepsilon}_n\} &= \text{Var}\left\{(\alpha_{\ll n, \bullet} - \tilde{\alpha}_{\ll n, \bullet})^2\right\} \\ &= \text{Var}\left\{\alpha_{\ll n, \bullet}^2 - 2\alpha_{\ll n, \bullet}\tilde{\alpha}_{\ll n, \bullet} + \tilde{\alpha}_{\ll n, \bullet}^2\right\} \\ &= \text{Var}\left\{-2\alpha_{\ll n, \bullet}\tilde{\alpha}_{\ll n, \bullet} + \tilde{\alpha}_{\ll n, \bullet}^2\right\} \\ &= \text{Var}\left\{-2\alpha_{\ll n, \bullet}\tilde{\alpha}_{\ll n, \bullet}\right\} + \text{Var}\left\{\tilde{\alpha}_{\ll n, \bullet}^2\right\} + \text{Cov}\left\{-2\alpha_{\ll n, \bullet}\tilde{\alpha}_{\ll n, \bullet}, \tilde{\alpha}_{\ll n, \bullet}^2\right\} \\ &= 4\alpha_{\ll n, \bullet}^2 \text{Var}\{\tilde{\alpha}_{\ll n, \bullet}\} + \text{Var}\left\{\tilde{\alpha}_{\ll n, \bullet}^2\right\} - 2\alpha_{\ll n, \bullet} \text{Cov}\left\{\tilde{\alpha}_{\ll n, \bullet}, \tilde{\alpha}_{\ll n, \bullet}^2\right\} \\ &= 4\alpha_{\ll n, \bullet}^2 \left( \mathbb{E}\left\{\tilde{\alpha}_{\ll n, \bullet}^2\right\} - \mathbb{E}\left\{\tilde{\alpha}_{\ll n, \bullet}\right\}^2 \right) + \left( \mathbb{E}\left\{\tilde{\alpha}_{\ll n, \bullet}^4\right\} - \mathbb{E}\left\{\tilde{\alpha}_{\ll n, \bullet}^2\right\}^2 \right) \\ &\quad - 2\alpha_{\ll n, \bullet} \mathbb{E}\left\{(\tilde{\alpha}_{\ll n, \bullet} - \mathbb{E}\left\{\tilde{\alpha}_{\ll n, \bullet}\right\})(\tilde{\alpha}_{\ll n, \bullet}^2 - \mathbb{E}\left\{\tilde{\alpha}_{\ll n, \bullet}^2\right\})\right\} \end{aligned}$$

<sup>19</sup>The rank of a Hermitian matrix is identical to its non-zero eigenvalues, since every Hermitian matrix can be diagonalized with its eigenvalues as diagonal elements. Furthermore, since eigenvalues and eigenvectors are transformation-invariant and the rank of a diagonal matrix is the number of non-zero column vectors, the preceding statement is proved.

$$\begin{aligned}
&= 4\alpha_{\triangleleft n, \bullet}^2 \left( \mathbb{E}\{\tilde{\alpha}_{\triangleleft n, \bullet}^2\} - \mathbb{E}\{\tilde{\alpha}_{\triangleleft n, \bullet}\}^2 \right) + \left( \mathbb{E}\{\tilde{\alpha}_{\triangleleft n, \bullet}^4\} - \mathbb{E}\{\tilde{\alpha}_{\triangleleft n, \bullet}^2\}^2 \right) \\
&\quad - 2\alpha_{\triangleleft n, \bullet} \mathbb{E}\{\tilde{\alpha}_{\triangleleft n, \bullet}^3\} - \mathbb{E}\{\tilde{\alpha}_{\triangleleft n, \bullet}^2\} \tilde{\alpha}_{\triangleleft n, \bullet} - \mathbb{E}\{\tilde{\alpha}_{\triangleleft n, \bullet}\} \tilde{\alpha}_{\triangleleft n, \bullet}^2 + \mathbb{E}\{\tilde{\alpha}_{\triangleleft n, \bullet}\} \mathbb{E}\{\tilde{\alpha}_{\triangleleft n, \bullet}^2\} \\
&= 4\alpha_{\triangleleft n, \bullet}^2 \left( \mathbb{E}\{\tilde{\alpha}_{\triangleleft n, \bullet}^2\} - \mathbb{E}\{\tilde{\alpha}_{\triangleleft n, \bullet}\}^2 \right) + \left( \mathbb{E}\{\tilde{\alpha}_{\triangleleft n, \bullet}^4\} - \mathbb{E}\{\tilde{\alpha}_{\triangleleft n, \bullet}^2\}^2 \right) \\
&\quad - 2\alpha_{\triangleleft n, \bullet} \mathbb{E}\{\tilde{\alpha}_{\triangleleft n, \bullet}^3\} + 2\alpha_{\triangleleft n, \bullet} \mathbb{E}\{\tilde{\alpha}_{\triangleleft n, \bullet}^2\} \mathbb{E}\{\tilde{\alpha}_{\triangleleft n, \bullet}\} \\
&\quad + 2\alpha_{\triangleleft n, \bullet} \mathbb{E}\{\tilde{\alpha}_{\triangleleft n, \bullet}\} \mathbb{E}\{\tilde{\alpha}_{\triangleleft n, \bullet}^2\} - 2\alpha_{\triangleleft n, \bullet} \mathbb{E}\{\tilde{\alpha}_{\triangleleft n, \bullet}\} \mathbb{E}\{\tilde{\alpha}_{\triangleleft n, \bullet}^2\} \\
&= 4\alpha_{\triangleleft n, \bullet}^2 \left( \mathbb{E}\{\tilde{\alpha}_{\triangleleft n, \bullet}^2\} - \mathbb{E}\{\tilde{\alpha}_{\triangleleft n, \bullet}\}^2 \right) + \left( \mathbb{E}\{\tilde{\alpha}_{\triangleleft n, \bullet}^4\} - \mathbb{E}\{\tilde{\alpha}_{\triangleleft n, \bullet}^2\}^2 \right) \\
&\quad - 2\alpha_{\triangleleft n, \bullet} \left( \mathbb{E}\{\tilde{\alpha}_{\triangleleft n, \bullet}^3\} - \mathbb{E}\{\tilde{\alpha}_{\triangleleft n, \bullet}\} \mathbb{E}\{\tilde{\alpha}_{\triangleleft n, \bullet}^2\} \right). \tag{73}
\end{aligned}$$

In the third equality, we use that an additive constant plays no role in the variance. We then decompose the variance of a sum into several individual variances and their associated covariance. In the sixth equation, we replace the variance by the known difference in expectations. In the remaining steps, we restructure.

Let the measurements of the incident angles additionally be Gaussian distributed according to

$$\tilde{\alpha}_{\triangleleft n, \bullet} \sim \mathcal{N}(\alpha_{\triangleleft n, \bullet}, \sigma_{\triangleleft n, \bullet}^2). \tag{74}$$

The moment-generating function for any Gaussian distribution  $\tilde{x} \sim \mathcal{N}(\mu, \sigma^2)$  reads [44]

$$m_{\tilde{x}}(t) = \exp\left(\mu t + \frac{1}{2}\sigma^2 t^2\right). \tag{75}$$

And thus, for the moments we have

$$\begin{aligned}
\mathbb{E}\{\tilde{x}^1\} &= m_{\tilde{x}}^{(1)}(0) = \mu \\
\mathbb{E}\{\tilde{x}^2\} &= m_{\tilde{x}}^{(2)}(0) = \mu^2 + \sigma^2 \\
\mathbb{E}\{\tilde{x}^3\} &= m_{\tilde{x}}^{(3)}(0) = \mu^3 + 3\mu\sigma^2 \\
\mathbb{E}\{\tilde{x}^4\} &= m_{\tilde{x}}^{(4)}(0) = \mu^4 + 6\mu^2\sigma^2 + 3\sigma^4. \tag{76}
\end{aligned}$$

Substituting and inserting this into (73), we finally obtain

$$\text{Var}\{\tilde{\varepsilon}_n\} = 2\sigma_{\triangleleft n, \bullet}^4. \tag{77}$$

## REFERENCES

- [1] Karim M. Abadir and Jan R. Magnus. 2005. *Matrix Algebra*. Cambridge University Press. DOI: <https://doi.org/10.1017/CBO9780511810800>
- [2] Monther Abusultan, Sam Harkness, Brock J. LaMeres, and Yikun Huang. 2010. FPGA implementation of a Bartlett direction of arrival algorithm for a 5.8 GHz circular antenna array. In *Proceedings of the 2010 IEEE Aerospace Conference*. 1–10. DOI: <https://doi.org/10.1109/AERO.2010.5446970>
- [3] Atmel. 2016. *Atmel AT86RF216 Device Family*. Atmel.
- [4] Ahmed Badawy, Tamer Khattab, Daniele Trinchero, Tarek El-Fouly, and Amr Mohamed. 2014. A simple AoA estimation scheme. *CoRR* 1409.5744 (2014).
- [5] Ahmed Badawy, Tamer Khattab, Daniele Trinchero, Tarek M. Elfouly, and Amr Mohamed. 2017. A simple cross correlation switched beam system (XSBS) for angle of arrival estimation. *IEEE Access* 5 (2017), 3340–3352. DOI: <https://doi.org/10.1109/ACCESS.2017.2669202>
- [6] A. Barabell. 1983. Improving the resolution performance of eigenstructure-based direction-finding algorithms. In *Proceedings of the IEEE International Conference on Acoustics, Speech, and Signal Processing (ICASSP'83)*, Vol. 8. 336–339. DOI: <https://doi.org/10.1109/ICASSP.1983.1172124>
- [7] M. S. Bartlett. 1950. Periodogram analysis and continuous spectra. *Biometrika* 37, 1-2 (1950), 1–16. DOI: <https://doi.org/10.1093/biomet/37.1-2.1>

- [8] J. Capon. 1969. High-resolution frequency-wavenumber spectrum analysis. *Proceedings of the IEEE* 57, 8 (1969), 1408–1418. DOI : <https://doi.org/10.1109/PROC.1969.7278>
- [9] Y. T. Chan, F. Chan, W. Read, B. R. Jackson, and B. H. Lee. 2014. Hybrid localization of an emitter by combining angle-of-arrival and received signal strength measurements. In *Proceedings of the 2014 IEEE 27th Canadian Conference on Electrical and Computer Engineering (CCECE'14)*. 1–5. DOI : <https://doi.org/10.1109/CCECE.2014.6900968>
- [10] J. L. Chau, D. L. Hysell, K. M. Kuyeng, and F. R. Galindo. 2008. Phase calibration approaches for radar interferometry and imaging configurations: Equatorial spread F results. *Annales Geophysicae* 26, 8 (2008), 2333–2343. DOI : <https://doi.org/10.5194/angeo-26-2333-2008>
- [11] Hsieh-Chung Chen, Tsung-Han Lin, H. T. Kung, Chit-Kwan Lin, and Youngjune Gwon. 2012. Determining RF angle of arrival using COTS antenna arrays: A field evaluation. In *Proceedings of the 2012 IEEE Military Communications Conference (MILCOM'12)*. 1–6. DOI : <https://doi.org/10.1109/MILCOM.2012.6415851>
- [12] Jin-Feng Chen and Hong Ma. 2011. An accurate real-time algorithm for spectrum peaks search in 2D MUSIC. In *Proceedings of the 2011 International Conference on Multimedia Technology*. 3385–3388. DOI : <https://doi.org/10.1109/ICMT.2011.6001931>
- [13] K. W. Cheung, H. C. So, W.-K. Ma, and Y. T. Chan. 2006. A constrained least squares approach to mobile positioning: Algorithms and optimality. *EURASIP Journal on Applied Signal Processing* 2006, 20858 (2006), 1–23. DOI : <https://doi.org/10.1155/ASP/2006/20858>
- [14] Adrian Figueiroa. 2021. *Advanced System Architectures and Processing Algorithms for Digital Beamforming Radars*. Vogt.
- [15] W. A. Gardner. 1988. Simplification of MUSIC and ESPRIT by exploitation of cyclostationarity. *Proceedings of the IEEE* 76, 7 (1988), 845–847. DOI : <https://doi.org/10.1109/5.7152>
- [16] L. Gazzah, L. Najjar, and H. Besbes. 2015. Selective hybrid RSS/AOA approximate maximum likelihood mobile intra cell localization. In *Proceedings of the 2015 European Wireless Conference (EW'15)*. 1–6.
- [17] L. C. Godara. 1997. Application of antenna arrays to mobile communications, part II: Beam-forming and direction-of-arrival considerations. *Proceedings of the IEEE* 85, 8 (1997), 1195–1245. DOI : <https://doi.org/10.1109/5.622504>
- [18] Konstantinos A. Gotsis, Katherine Siakavara, and John N. Sahalos. 2009. On the direction of arrival (DoA) estimation for a switched-beam antenna system using neural networks. *IEEE Transactions on Antennas and Propagation* 57, 5 (2009), 1399–1411. DOI : <https://doi.org/10.1109/TAP.2009.2016721>
- [19] Marco Gunia, Florian Protze, Niko Joram, and Frank Ellinger. 2016. Setting up an ultra-wideband positioning system using off-the-shelf components. In *Proceedings of the 2016 13th Workshop on Positioning, Navigation, and Communications (WPNC'16)*. 1–6. DOI : <https://doi.org/10.1109/WPNC.2016.7822860>
- [20] Marco Gunia, Bo Zhang, Niko Joram, and Frank Ellinger. 2016. A hybrid localization framework supporting multiple standards and manifold post-processing. In *Proceedings of the 2016 International Conference on Localization and GNSS (ICL-GNSS'16)*. 1–6. DOI : <https://doi.org/10.1109/ICL-GNSS.2016.7533835>
- [21] Marco Gunia, Adrian Zinke, Niko Joram, and Frank Ellinger. 2017. Setting up a phase-based positioning system using off-the-shelf components. In *Proceedings of the 14th Workshop on Positioning, Navigation, and Communications (WPNC'17)*. IEEE, Los Alamitos, CA, 1–6. DOI : <https://doi.org/10.1109/WPNC.2017.8250065>
- [22] Marco Gunia, Adrian Zinke, Niko Joram, and Frank Ellinger. 2019. Hardware design for an angle of arrival positioning system. In *Proceedings of the 4th KuVS/GI Expert Talk on Localization (EToL'19)*. 1–3.
- [23] Katsuyuki Haneda, Ken Ichi Takizawa, Jun Ichi Takada, Marzieh Dashti, and Pertti Vainikainen. 2009. Performance evaluation of threshold-based UWB ranging methods—Leading edge vs. search back -. In *Proceedings of the 2009 3rd European Conference on Antennas and Propagation*. 3673–3677.
- [24] Adam Helman. 2005. *The Finest Peaks: Prominence and Other Mountain Measures*. Trafford Publishing.
- [25] Kang Hu, Chaojie Gu, and Jiming Chen. 2022. LTrack: A LoRa-based indoor tracking system for mobile robots. *IEEE Transactions on Vehicular Technology* 71, 4 (2022), 4264–4276. DOI : <https://doi.org/10.1109/TVT.2022.3143526>
- [26] L. Huang, H. Chen, Y. Chen, and H. Xin. 2016. Research of DOA estimation based on MUSIC algorithm. In *Proceedings of the 2016 6th International Conference on Machinery, Materials, Environment, Biotechnology, and Computer*. DOI : <https://doi.org/10.2991/mmebc-16.2016.432>
- [27] Md. Tamzeeb Islam and Shahriar Nirjon. 2021. WiDeo: One shot domain adaptation for cross-environment WiFi-based activity classification through RF-visual joint embedding. In *Proceedings of the 2021 17th International Conference on Distributed Computing in Sensor Systems (DCOSS'21)*. 69–71. DOI : <https://doi.org/10.1109/DCOSS52077.2021.00025>
- [28] Mahdi Jalali, Mohamad Naser Moghaddasi, and Alireza Habibzadeh. 2009. Comparing accuracy for ML, MUSIC, ROOT-MUSIC and spatially smoothed algorithms for 2 users. In *Proceedings of the 2009 Mediterranean Microwave Symposium (MMS'09)*. 1–5. DOI : <https://doi.org/10.1109/MMS.2009.5409832>
- [29] Youssef Khmou, Safi Said, and Miloud Frikel. 2014. Comparative study between several direction of arrival estimation methods. *Journal of Telecommunications and Information Technology* 2014 (2014), 41–48.

- [30] Minseok Kim, K. Ichige, and H. Arai. 2003. Implementation of FPGA based fast DOA estimator using unitary MUSIC algorithm [cellular wireless base station applications]. In *Proceedings of the 2003 IEEE 58th Vehicular Technology Conference (VTC 2003-Fall)*. 213–217. DOI : <https://doi.org/10.1109/VETECF.2003.1285009>
- [31] Manikanta Kotaru, Kiran Joshi, Dinesh Bharadia, and Sachin Katti. 2015. SpotFi: Decimeter level localization using WiFi. In *Proceedings of the 2015 ACM Conference of the Special Interest Group on Data Communication (SIGCOMM'15)*. DOI : <https://doi.org/10.1145/2785956.2787487>
- [32] Michael J. Kuhn, Jonathan Turnmire, Mohamed R. Mahfouz, and Aly E. Fathy. 2010. Adaptive leading-edge detection in UWB indoor localization. In *Proceedings of the 2010 IEEE Radio and Wireless Symposium*. 268–271. DOI : <https://doi.org/10.1109/RWS.2010.5434259>
- [33] Ramdas Kumaresan and Donald W. Tufts. 1983. Estimating the angles of arrival of multiple plane waves. *IEEE Transactions on Aerospace and Electronic Systems AES-19*, 1 (1983), 134–139. DOI : <https://doi.org/10.1109/TAES.1983.309427>
- [34] T. B. Lavate, V. K. Kokate, and A. M. Sapkal. 2010. Performance analysis of MUSIC and ESPRIT DOA estimation algorithms for adaptive array smart antenna in mobile communication. In *Proceedings of the 2010 2nd International Conference on Computer and Network Technology*. 308–311. DOI : <https://doi.org/10.1109/ICCNT.2010.45>
- [35] Charles L. Lawson and Richard J. Hanson. 1987. *Solving Least Squares Problems*. Society of Industrial and Applied Mathematics.
- [36] Bernard W. Lindgren. 1976. *Statistical Theory* (ed.). Macmillan.
- [37] Roderick Little and Donald B. Rubin. 2002. *Statistical Analysis with Missing Data* (2nd ed.). Wiley-Interscience.
- [38] Jun Liu, Jiayao Gao, Sanjay Jha, and Wen Hu. 2021. Seirios: Leveraging multiple channels for LoRaWAN indoor and outdoor localization. In *Proceedings of the 27th Annual International Conference on Mobile Computing and Networking (MobiCom'21)*. 656–669. DOI : <https://doi.org/10.1145/3447993.3483256>
- [39] John Makhoul. 1975. Linear prediction: A tutorial review. *Proceedings of the IEEE* 63, 4 (1975), 561–580. DOI : <https://doi.org/10.1109/PROC.1975.9792>
- [40] Robert J. Marks II. 2009. *Handbook of Fourier Analysis & Its Applications*. Oxford University Press.
- [41] D. Neiryck, M. O'Duinn, and C. McElroy. 2015. Characterisation of the NLOS performance of an IEEE 802.15.4a receiver. In *Proceedings of the 12th Workshop on Positioning Navigation and Communication (WPNC'15)*. 1–4.
- [42] James L. Melsa and Andrew P. Sage. 2013. *Introduction to Probability and Stochastic Processes*. Dover Publications.
- [43] M. Mohanna, M. L. Rabeh, E. M. Zieur, and S. Hekala. 2013. Optimization of MUSIC algorithm for angle of arrival estimation in wireless communications. *NRIAG Journal of Astronomy and Geophysics* 2, 1 (2013), 116–124. DOI : <https://doi.org/10.1016/j.nrjag.2013.06.014>
- [44] A. M. Mood. 1950. *Introduction to the Theory of Statistics*. McGraw-Hill.
- [45] Christian Morhart, Erwin Biebl, Daniel Schwarz, and Ralph Rasshofer. 2009. Cooperative multi-user detection and localization for pedestrian protection. In *Proceedings of the 2009 German Microwave Conference*. 1–5. DOI : <https://doi.org/10.1109/GEMIC.2009.4815863>
- [46] A. Pages-Zamora, J. Vidal, and D. H. Brooks. 2002. Closed-form solution for positioning based on angle of arrival measurements. In *Proceedings of the 13th IEEE International Symposium on Personal, Indoor, and Mobile Radio Communications*, Vol. 4. 1522–1526. DOI : <https://doi.org/10.1109/PIMRC.2002.1045433>
- [47] Kun Il Park. 2018. *Fundamentals of Probability and Stochastic Processes with Applications to Communications*. Springer.
- [48] M. Pelka, C. Bollmeyer, and H. Hellbrück. 2014. Accurate radio distance estimation by phase measurements with multiple frequencies. In *Proceedings of the 2014 International Conference on Indoor Positioning and Indoor Navigation (IPIN'14)*. 142–151. DOI : <https://doi.org/10.1109/IPIN.2014.7275478>
- [49] V. F. Pisarenko. 1973. The retrieval of harmonics from a covariance function. *Geophysical Journal International* 33, 3 (1973), 347–366. DOI : <https://doi.org/10.1111/j.1365-246X.1973.tb03424.x>
- [50] Chongying Qi, Zhijie Chen, Yongliang Wang, and Yongshun Zhang. 2007. DOA estimation for coherent sources in unknown nonuniform noise fields. *IEEE Transactions on Aerospace and Electronic Systems* 43, 3 (2007), 1195–1204. DOI : <https://doi.org/10.1109/TAES.2007.4383611>
- [51] S. S. Reddi. 1979. Multiple source location-a digital approach. *IEEE Transactions on Aerospace and Electronic Systems AES-15*, 1 (1979), 95–105. DOI : <https://doi.org/10.1109/TAES.1979.308800>
- [52] R. Roy and T. Kailath. 1989. ESPRIT-estimation of signal parameters via rotational invariance techniques. *IEEE Transactions on Acoustics, Speech, and Signal Processing* 37, 7 (1989), 984–995. DOI : <https://doi.org/10.1109/29.32276>
- [53] R. Schmidt. 1986. Multiple emitter location and signal parameter estimation. *IEEE Transactions on Antennas and Propagation* 34, 3 (1986), 276–280. DOI : <https://doi.org/10.1109/TAP.1986.1143830>
- [54] Souvik Sen, Jeongkeun Lee, Kyu-Han Kim, and Paul Congdon. 2013. Avoiding multipath to revive inbuilding WiFi localization. In *Proceedings of the 11th Annual International Conference on Mobile Systems, Applications, and Services*. DOI : <https://doi.org/10.1145/2462456.2464463>

- [55] Tie-Jun Shan, M. Wax, and T. Kailath. 1985. On spatial smoothing for direction-of-arrival estimation of coherent signals. *IEEE Transactions on Acoustics, Speech, and Signal Processing* 33, 4 (1985), 806–811. DOI : <https://doi.org/10.1109/TASSP.1985.1164649>
- [56] Chen Sun and Nemai Karmakar. 2004. Direction of arrival estimation based on a single port smart antenna using MUSIC algorithm with periodic signals. *International Journal of Signal Processing* 1, 2 (2004), 153–161.
- [57] Gangcan Sun, Xuefei Xu, and Kai Yang. 2012/11. Angle-of-arrival based constrained total least-squares location algorithm. In *Proceedings of the 2012 National Conference on Information Technology and Computer Science*. 781–783. DOI : <https://doi.org/10.2991/citcs.2012.198>
- [58] Yue Sun, Duoli Zhang, Pingping Li, Rui Jiao, and Bin Zhang. 2014. The studies and FPGA implementation of spectrum peak search in MUSIC algorithm. In *Proceedings of the 2014 International Conference on Anti-Counterfeiting, Security, and Identification (ASID'14)*. 1–5. DOI : <https://doi.org/10.1109/ICASID.2014.7064967>
- [59] H. Tang. 2019. *DOA Estimation Based on MUSIC Algorithm*. Linné-Universität.
- [60] P. Tarrio, A. M. Bernardo, and J. R. Casar. 2011. Weighted least squares techniques for improved received signal strength based localization. *Sensors* 2011 11, 9 (2011), 8569–8592. DOI : <https://doi.org/10.3390/s110908569>
- [61] Don J. Torrieri. 1984. Statistical theory of passive location systems. *IEEE Transactions on Aerospace and Electronic Systems AES-20*, 2 (1984), 183–198. DOI : <https://doi.org/10.1109/TAES.1984.310439>
- [62] V. Y. Vu, A. J. Braga, X. Begaud, and B. Huyart. 2005. Measurement of direction-of-arrival of coherent signals using five-port reflectometers and quasi-Yagi antennas. *IEEE Microwave and Wireless Components Letters* 15, 9 (2005), 558–560. DOI : <https://doi.org/10.1109/LMWC.2005.855391>
- [63] Sichun Wang, Brad R. Jackson, and Robert Inkol. 2012. Hybrid RSS/AOA emitter location estimation based on least squares and maximum likelihood criteria. In *Proceedings of the 2012 26th Biennial Symposium on Communications (QBSC'12)*. 24–29. DOI : <https://doi.org/10.1109/QBSC.2012.6221344>
- [64] Zhangsheng Wang, Wei Xie, Yanbin Zou, and Qun Wan. 2019. DOA estimation using single or dual reception channels based on cyclostationarity. *IEEE Access* 7 (2019), 54787–54795. DOI : <https://doi.org/10.1109/ACCESS.2019.2912907>
- [65] Stijn Wielandt and Lieven De Strycker. 2017. Indoor multipath assisted angle of arrival localization. *Sensors* 2017 17, 11 (2017), 2522. DOI : <https://doi.org/10.3390/s17112522>
- [66] Meng Xiangwei, Guan Jian, and He You. 2003. Performance analysis of the weighted window CFAR algorithms. In *Proceedings of the 2003 International Conference on Radar*. 354–357. DOI : <https://doi.org/10.1109/RADAR.2003.1278766>
- [67] Adrian Zinke. 2018. *Analyse der Realisierbarkeit der Integration eines phasen-basierten Lokalisierungssystems in ein vorhandenes FMCW-Radarsystem*. Technische Universität Dresden.

Received 3 January 2022; revised 30 November 2022; accepted 15 December 2022